



HAL
open science

Local buckling on large sandwich panels applied to light aviation: Experimental and computation dialogue

M. Ginot, C. Bouvet, B. Castanié, M. d'Ottavio, Joël Serra, N. Mahuet

► To cite this version:

M. Ginot, C. Bouvet, B. Castanié, M. d'Ottavio, Joël Serra, et al.. Local buckling on large sandwich panels applied to light aviation: Experimental and computation dialogue. *International Journal of Solids and Structures*, 2023, 268, pp.112170. 10.1016/j.ijsolstr.2023.112170 . hal-04080624

HAL Id: hal-04080624

<https://hal.science/hal-04080624>

Submitted on 25 Apr 2023

HAL is a multi-disciplinary open access archive for the deposit and dissemination of scientific research documents, whether they are published or not. The documents may come from teaching and research institutions in France or abroad, or from public or private research centers.

L'archive ouverte pluridisciplinaire **HAL**, est destinée au dépôt et à la diffusion de documents scientifiques de niveau recherche, publiés ou non, émanant des établissements d'enseignement et de recherche français ou étrangers, des laboratoires publics ou privés.

1 **Local buckling on large sandwich panels applied to light aviation:**

2 **Experimental and computation dialogue.**

3 M. Ginot^{a,b}, C. Bouvet^b, B. Castanié^{b,*}, M. D'Ottavio^c, J. Serra^b, N. Mahuet^a

4 ^a Elixir Aircraft, Rue du Jura, 17000 La Rochelle, France

5 ^b Institut Clément Ader (ICA), Université de Toulouse, CNRS UMR 5312, INSA, ISAE-Supaéro,
6 INSA, IMT Mines Albi, UPS, Toulouse, France

7 ^c LEME – EA4416, Université Paris Nanterre, 50, Rue de Sèvres, 92410 Ville d'Avray, France

8 * Corresponding author: bruno.castanie@insa-toulouse.fr

9 **Keywords:** Sandwich structures; Local buckling; Wrinkling; Structural testing; Experimental
10 and computation dialogue; nonlinear FEM.

11 **Abstract**

12 Wrinkling is a local buckling phenomenon in sandwich structures subjected to compression
13 and shear loading **that** is challenging for the **aircraft** design engineer. Numerous wrinkling
14 models are proposed in the literature **but** historical formulas developed after the Second
15 World War are **still widely used by the industry with important knock down factors**. Theory-
16 experiment correlation should be the final step in validating and evaluating the models. This
17 article **presents an experimental-computational dialogue** on structural tests on large
18 sandwich panels of dimensions 558 x 536 mm² representative of the design used in light
19 aviation. The panels were subjected to compressive and shear loading by using the VERTEX
20 test bench and wrinkling failures were observed. Comparisons are first made with linear

21 wrinkling models. Despite correlations are quite encouraging, the imperfection-sensitivity of
22 the experimentally observed wrinkling failure questions the pertinence of a linear bifurcation
23 approach. A nonlinear Finite Element Model (FEM) of the sandwich panels is then developed.
24 Initial imperfections measured by Stereo Digital Image Correlation (SDIC) are directly
25 introduced in the mesh and an elastoplastic constitutive law for the core is implemented.
26 Dynamic explicit computation is used to access the highly nonlinear ~~post-buckling~~ behaviour
27 and matches the test observations very well. The nonlinear FEM provides an improved,
28 conservative prediction of wrinkling loads over the linear models.

29 1 Introduction

30 Wrinkling is a local instability that can occur when a sandwich structure is subjected to
31 compression or shear loading. The length of the wrinkle pattern is of the order **of magnitude**
32 of the thickness of the sandwich. Wrinkling is considered a primary cause of failure in sandwich
33 structures with thin skins and low core characteristics, such as the configurations used in light
34 aviation. Wrinkling models have been under development since the Second World War and
35 several literature reviews retrace the evolution of wrinkling modelling (Castanié et al., 2020;
36 Ley et al., 1999; Ginot et al., 2021). Without being exhaustive, the first historical formulas were
37 developed with hypotheses using isotropic skins on an elastic foundation in a 2D framework
38 (Hoff and Mautner, 1945; Plantema, 1966; Allen, 1969). More recent works achieved unified
39 models capable of describing global and local buckling modes in sandwich structures (Benson
40 and Mayers, 1967; Leotoing, 2001; Niu and Talreja, 1999; Douville and Le Grogneq, 2013).
41 Other models have been enriched by adding orthotropy for the skin (Fagerberg and Zenkert,
42 2005a) and for the core (Vonach and Rammerstorfer, 2000) and the possibility of a multiaxial

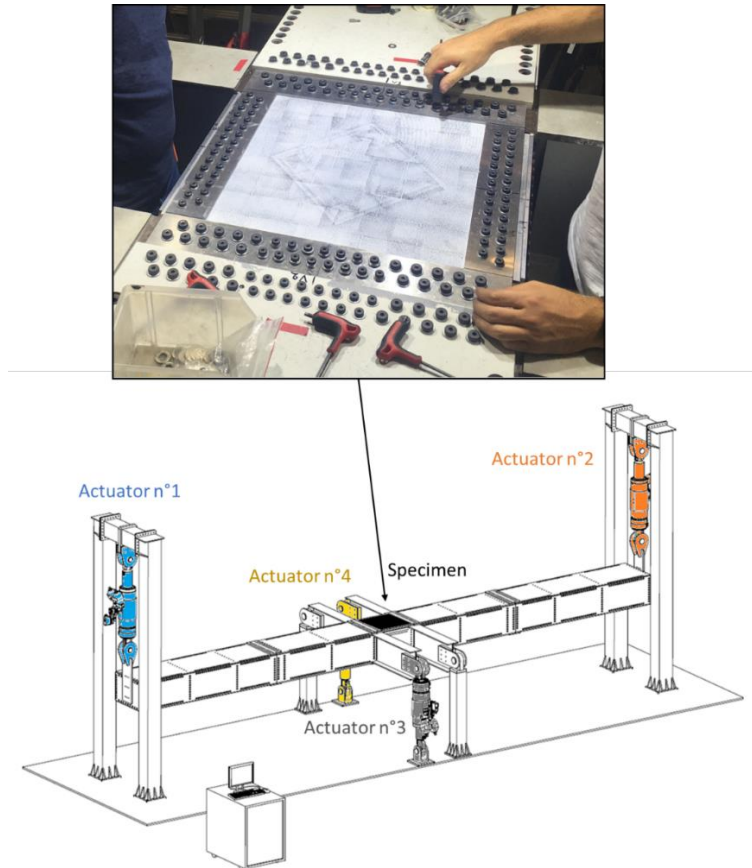
43 loading (Sullins et al., 1969; Birman and Bert, 2004). **Eventually, few** authors have proposed
44 higher order formulations with numerical resolutions. An interesting approach is the
45 Sublaminar Generalised Unified Formulation (S.G.U.F) developed by D'Ottavio (2016). Based
46 on a variable kinematic approach, the formulation allows dedicated models to be introduced
47 for skins and core, thus allowing to choose and identify the model required for properly
48 grasping global and/or local response depending on the problem considered (D'Ottavio et al.,
49 2016; Vescovini et al., 2018). To a lesser extent in the literature, **experimental-computational**
50 **dialogues** on sandwich structures have been achieved. Thomsen et al. (1996a; 1996b) worked
51 on the influence of the ply drops on sandwich beams with honeycomb core from an enhanced
52 Winkler model. Out-of-plane skin displacement has been solved numerically. Fagerberg (2004;
53 Fagerberg and Zenker 2005a) carried out important test campaigns on sandwich panels, and
54 his results have been used as a reference for the validation of several wrinkling models
55 (Fagerberg and Zenkert, 2005a; Fagerberg and Zenkert, 2005b). At the structure scale, Tuwair
56 et al. (2016) conducted a test on a sandwich panel under four point bending. Correlations
57 were performed with finite-element analyses and analytical models. Tuwair et al. (2016) noted
58 that using analytical approaches to find an exact solution for wrinkling problems may be
59 limited by the assumptions adopted for these methods. This remark is far from new. After a
60 test campaign, Hoff and Mautner (1945) recommended a knock down factor for their
61 analytical solution. This was taken up by Zenkert's sandwich construction handbook (1997)
62 and NASA's technical documents of the late 1960s (Sullins et al., 1969). Most of the
63 experimental results on wrinkling show that the classical formulas provide correct trends but
64 with a non-conservative load prediction (Hoff and Mautner, 1945; Norris, 1964). Therefore,
65 the aeronautic industry often uses the knock down factor recommended by Hoff and Mautner

66 to cover this complex phenomenon. The main reason why the analytical expressions are not
67 conservative is that the initial imperfections and displacements before buckling are not
68 considered. **The quantification of the effect of these imperfections is difficult especially in**
69 **the structural cases presented in this study. According to Fagerberg and Zenkert (2005a), in**
70 **the case of non-negligible imperfections (with an amplitude of the order of magnitude of**
71 **1/10th of the face sheet thickness), the out-of-plane displacement before buckling will be**
72 **significant and will increase significantly the non-linear behaviour of the structure.**
73 Therefore, Finite Element Models (FEM) often provide a more accurate way of taking
74 geometric and/or mechanical non-linearity into account and investigating the post-wrinkling
75 behaviour.

76 Several approaches can be followed to model a sandwich structure by commercial FE
77 packages. The use of an equivalent single layer model by means of shell elements with a
78 composite section is the less expensive approach but it is inapplicable for wrinkling studies
79 because it discards the out-of-plane deformation of the core. A three-layer model should thus
80 be adopted, where the core is modelled by continuum elements in order to retain its out-of-
81 plane response required for wrinkling analysis. The skins may be modelled by shell elements
82 or by continuum elements, the former approach being computationally more advantageous
83 due to the thinness of the skins, which would require too small continuum elements for
84 avoiding excessive element aspect ratios (Léotoing et al., 2002). Convergence studies
85 performed by Léotoing et al. (2002) also recommended to use a mesh density such that each
86 wavelength of the wrinkling pattern is discretized by at least 8 linear elements. **For this**
87 **matter, a preliminary analytical computation of the expected wavelength is of great help to**
88 **select a first mesh density.**

89 In the literature, models are too often compared to textbook cases – either directly via finite
90 element models, with no geometric defects and perfect boundary conditions (Ginot et al.,
91 2021), or via coupon scale tests that are simple to implement but suffer from underlying
92 boundary condition problems (Ley et al., 1999). A preceeding paper (Ginot et al., 2023) on the
93 subject presents wrinkling tests under multiaxial stresses at the plate scale. Five sandwich
94 panels were tested under compressive and shear loading with the VERTEX test bench (Figure
95 1) and wrinkling type failure was observed. The sandwich panel configurations were chosen
96 to be consistent with the sandwich structures used in light aviation (Castanié et al., 2020; Elixir
97 Aircraft). The VERTEX test bench (Figure 1) develops boundary conditions representative of
98 what an aeronautic sandwich panel can undergo in real conditions (Serra et al., 2017a). **This**
99 **experimental campaign provided a large number of valuable data concerning wrinkling of**
100 **built-up structures. The present paper thus presents an original and enhanced dialogue**
101 **between experimental testing and computational modelling; the novelty resides in the**
102 **consideration of the wrinkling phenomenon at the structural scale within an industry-**
103 **oriented context related to light aviation, which allows to shed light on various aspects**
104 **influencing this critical failure mode.**

105 The paper is organized as follows. **First**, the material, methods and results of the VERTEX test
106 campaign discussed in (Ginot et al., 2023) are summarised for presenting a self-contained
107 paper. Subsequently, the **experimental-computational dialogue** is presented in two main
108 parts: (1) Comparisons are made with linear wrinkling models, results and limits being
109 discussed, and (2) an advanced FEM is developed and the nonlinear analysis is compared to
110 the test results. **Eventually**, conclusions are drawn.



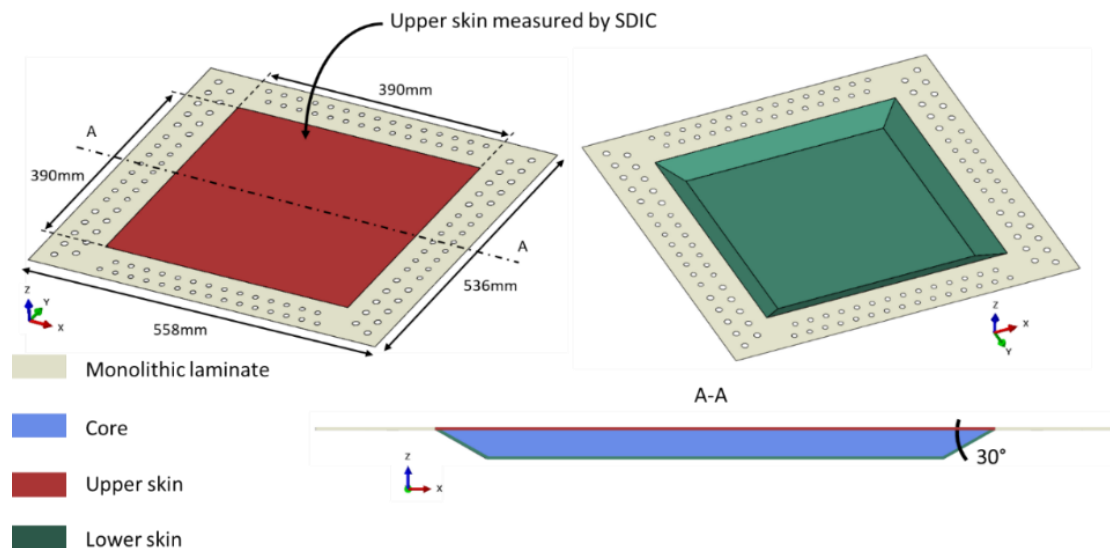
111

112 *Figure 1: VERTEX test bench and details of a specimen bolted onto the upper part of the*
 113 *central box.*

114 2 Materials, method, and test results

115 2.1 Materials and method

116 The operating principle of the VERTEX machine involves four hydraulic actuators used to load
 117 a rectangular box structure. The panel under test closes the upper part of the central box
 118 (Figure 1). Actuators 1 and 2 can push or pull symmetrically to bend the box structure of the
 119 bench, thus locally loading the tested panel in tension or compression. Similarly, actuators 3
 120 and 4 can push to twist the centre of the box structure, thus locally loading the tested panel
 121 in shear. The specimens used here were sandwich panels with a monolithic peripheral area
 122 and an asymmetric sandwich central area including a tapered region. As a result, the edges
 123 were monolithic and were drilled to bolt the specimen to the VERTEX test bench (Figure 2).



124

125

Figure 2: Overall panel geometry.

126 The specimen was positioned as shown in Figure 1 and bolted on its 4 sides with 128 screws.

127 The external dimensions were 558 x 536 mm², and the sandwich area with the tapered regions

128 was 390 x 390 mm² and about 21 mm thick (core and skins). The materials used for the

129 specimens were a Polymethacrylimide (PMI) foam of density 51 kg/m³ and prepreg

130 carbon/epoxy woven fabric with additional unidirectional prepreg in the F51_D2 sandwich

131 configuration. The nominal stacking sequences are shown in Table 1. A "one-shot/co-cured"

132 process was used in an autoclave. **Specimens** were tested under **either** compressive **loading**

133 or shear **loading** (Ginot et al., 2023). Three of the five specimens tested in (Ginot et al., 2023)

134 are studied in the present paper.

135 The observable surface was the upper skin; the lower skin faced the inner test bench box

136 structure. To locate wrinkling in the upper skin, an asymmetric geometry was used to create

137 an offset between the load introduction axis and the mean geometric plane of the sandwich

138 structure. It led to a bending moment and induced an additional compressive load in the upper

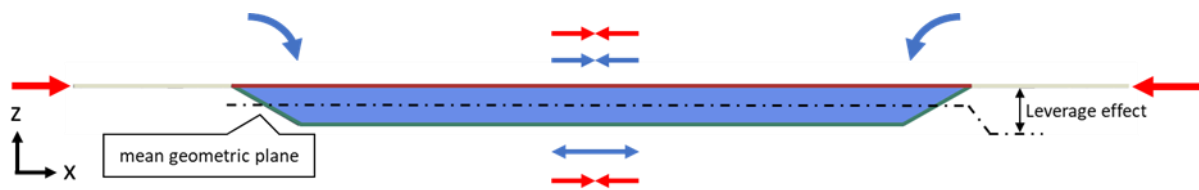
139 skin and a tensile load in the lower skin. The upper skin was thus more loaded and was liable

140 to buckle.

141 Table 1: Specimen stacking sequence in nominal area. Specimen nomenclature is F51_... for 51
 142 kg/m³ PMI foam and ..._Dx for specified stacking sequence.

| Specimen | F51_D1 | F51_D2 | F51_D3 |
|-------------------|----------------|----------------|----------------|
| Loading | Compressive | Compressive | Shear |
| Stacking sequence | Fabric +/- 45° | Fabric +/- 45° | Fabric +/- 45° |
| | | 2x Unidir 0° | |
| | Fabric 0°/90° | Fabric 0°/90° | Fabric +/- 45° |
| | PMI foam | PMI foam | PMI foam |
| | Fabric 0°/90° | Fabric 0°/90° | Fabric +/- 45° |
| | Fabric +/- 45° | Fabric +/- 45° | Fabric +/- 45° |
| | | | Fabric +/- 45° |

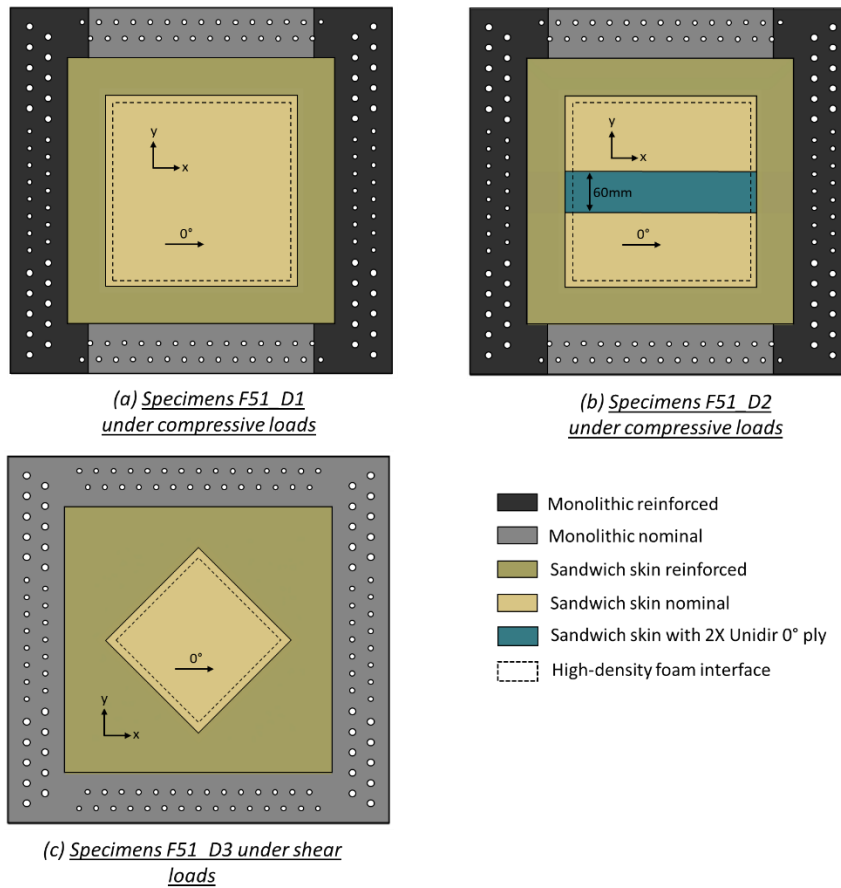
143



144

145 *Figure 3: Bending effect on asymmetric sandwich structure.*

146 To locate the wrinkling in the centre of the panel, a high-density foam frame was used to
 147 reinforce the tapered area. For the specimen under compressive loads, the nominal area was
 148 260 x 260 mm² (dotted frames in Figure 4 (a) and (b)).



149

150

Figure 4: Skin definition of the specimens.

151 Skins in the tapered area were reinforced (dark brown area in Figure 4). For the specimen

152 under shear loads, the nominal area (dotted frame in Figure 4 (c)) had a 172 x 172 mm²

153 **diamond** shape so as to have edges perpendicular to the principal stresses at **+/-45°**. For

154 specimen F51_D2, a 60 mm wide strip of 2X Unidirectional plies 0° ply was added (blue area

155 in Figure 4 (b)) as a typical stacking used in light aviation. The area where the stacking

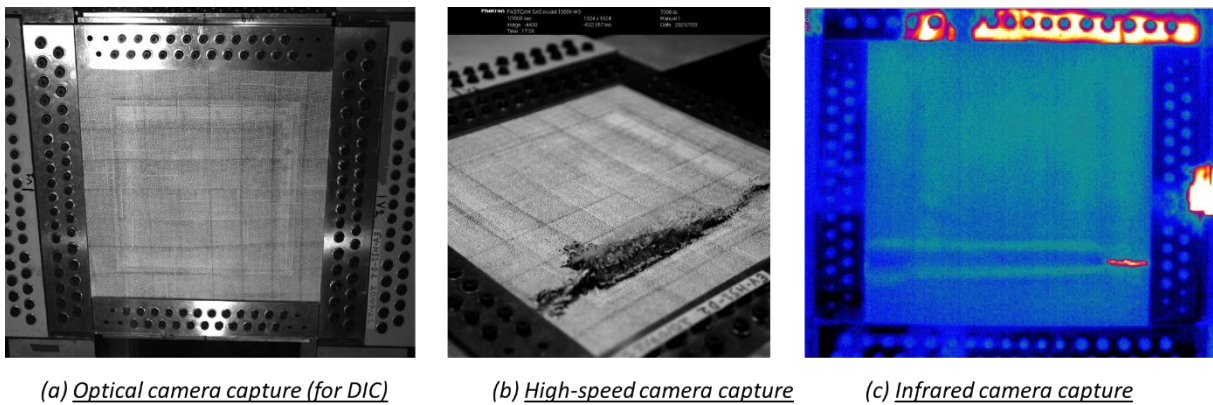
156 sequence corresponded to Table 1 was called the “nominal area” (light brown inside the

157 dotted frame area in Figure 4 (a) and (c) for specimens F51_D1 and F51_D3; blue area in Figure

158 4 (b) for specimens F51_D2).

159 2.2 Instrumentation

160 Stereo Digital Image Correlation (SDIC) with two 5 Mpx cameras was used, and a speckled
161 pattern was made on the upper face of the specimens (Figure 5 (a)). The acquisition frequency
162 was set to two images per second. Vic3D software (Correlated Solutions Inc., Columbia, SC,
163 USA) was used for post-processing. A high-speed camera (7000 fps) was **also** used to observe
164 a potential explosive failure (Figure 5 (b)). **An infrared camera was added** to the setup (Figure
165 5 (c)), allowing for possible wrinkling type failure measurements. In the lower skin, “Rosette”
166 gauges were used (the location of the gauges can be found in Ginot et al, 2023, figure 12).



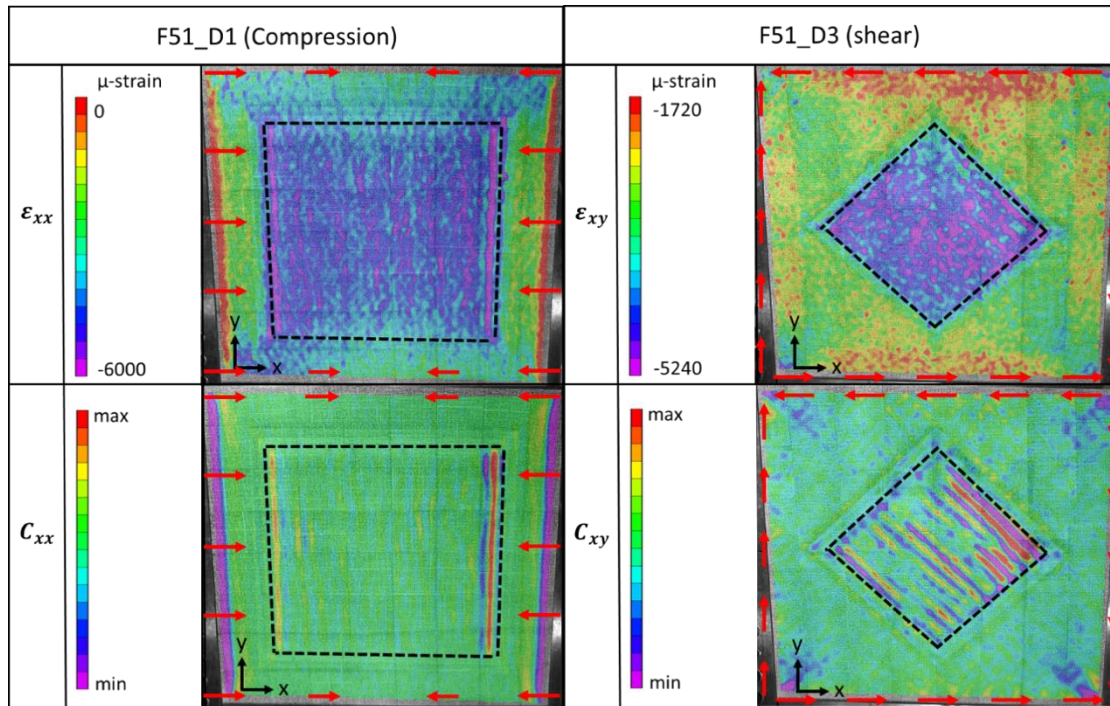
168 *Figure 5: Images captured by instrumentation cameras.*

169 2.3 Results

170 2.3.1 Strain and curvature fields

171 Figure 6 shows in-plane strains (ϵ_{xx} field of F51_D1 and ϵ_{xy} field of F51_D3). All the frames
172 were taken just before failure. A post-treatment is carried out in order to avoid the grained
173 noise characterizing the SDIC recordings in view of a clearer observation of the wrinkling
174 waves, see (Ginot et al, 2023) for more details. The waves of the wrinkling state do not
175 appear clearly and the whole plate remains under compression or shear respectively. The
176 strains are mainly uniform and follow typical expectations. Therefore, the curvature fields,

177 i.e. the inverse diameter of the circle locally tangent to the out-of-plane displacement are also
 178 shown Figure 6 (C_{xx} field of F51_D1 and C_{xy} field of F51_D3). The waves appear more clearly
 179 and are located near the boundaries of the central area for the compression case; For the
 180 shear case, waves are extensively present in the whole area of interest, but larger
 181 amplitudes are located near the boundaries also.



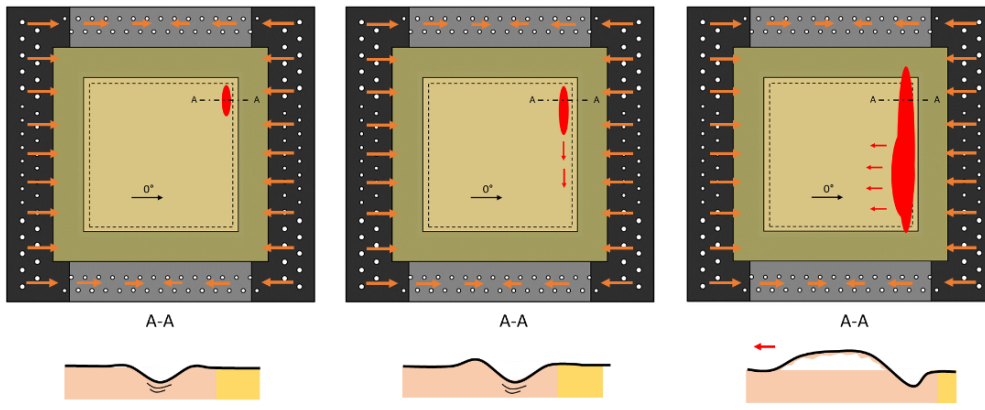
182 [---] Nominal area

183 *Figure 6: Strains and curvatures evolution fields obtained by SDIC just before failure in*
 184 *specimens F51_D1 and F51_D3.*

185 2.3.2 Failure scenario

186 For most specimens, the failure behaviour was similar (Figure 7). The specimens failed by
 187 wrinkling in the upper skin, thus validating the design of the specimens. **One or more**
 188 **wrinkling waves appeared provoking the core to crush locally. The wave eventually spread**
 189 **over the width with a failure of the core due to tension along the thickness direction. This**

190 lasted about 2 milliseconds starting from the core crushing. For the shear-loaded specimen,
191 the wrinkling wave followed the direction of the compressive principal stress.

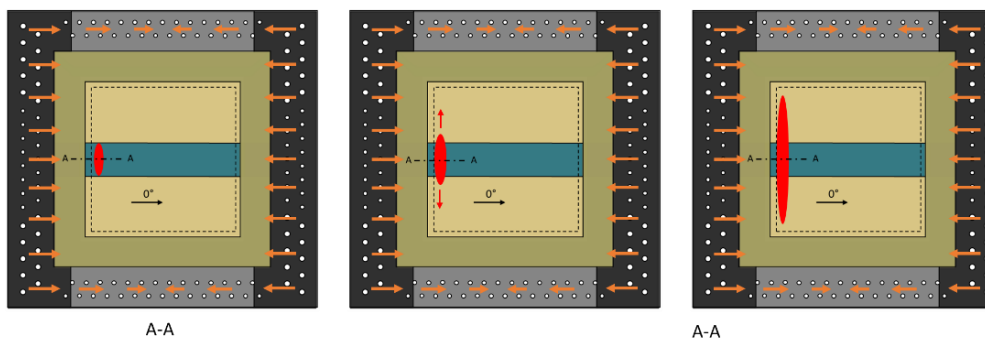


Wrinkling wave appears and core crushes locally

Wrinkling wave spreads over the width

Core fails in tension

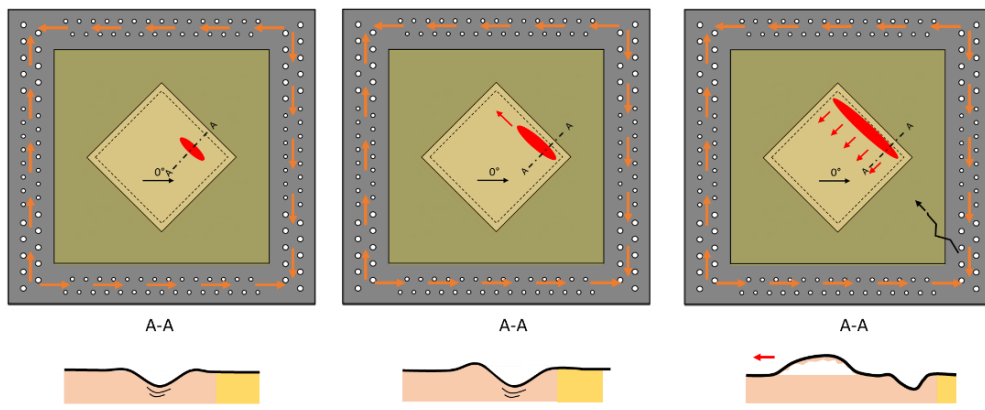
(a) *F51_D1 specimen*



Wrinkling wave appears and core crushes locally

Wrinkling wave spreads over the width, and core fails in tension

(c) *F51_D2 specimen*



Wrinkling wave appears and core crushes locally

Wrinkling wave spreads

Core fails in tension and wave moves on a large part of nominal area.

(b) *F51_D3 specimen*

Main loading direction
 PMI foam
 High-density foam
 Skin wave
 Skin static failure
 Nominal/High-density foam interface

192

193

Figure 7: Failure scenario for specimens F51_D1, F51_D2 and F51_D3.

194 2.4 Compressive and shear strains at failure

195 Table 2 lists the average principal compressive direction and compressive strain at failure of
 196 **the upper skin of the sandwich panel** in the nominal area for each specimen tested. The
 197 average compressive strain at specimen failure is measured thanks to SDIC (numerical
 198 extensometer) in the nominal area. For specimens under compressive loading, the principal
 199 compressive direction is not more than 4° from the x-axis, **which** can be considered as pure
 200 compression. For the specimen under shear loading, the principal compressive direction is
 201 about 52° from the x-axis whereas in a pure shear case it should be at 45°. This is due to a
 202 tensile component resulting from coupling between torsion and bending in the VERTEX bench.
 203 Therefore, the principal strain ε_2 is noted instead of the 45° strain. **Note that more**
 204 **information on the measurement method and parameters, the calculation of the average**
 205 **compressive or shear strains, are available in Ginot et al, 2023.**

206 *Table 2: Average strain at failure.*

| Specimen | F51_D1 | F51_D2 | F51_D3 |
|---------------------------------------|--|--|-------------------------------------|
| Loading | Compression | Compression | Shear |
| Failure type | wrinkling | wrinkling | wrinkling |
| Principal compressive direction | 3.9° | 3.6° | 51.8° |
| Average compressive strain at failure | $\varepsilon_{xx} = -5400 \mu$ strains | $\varepsilon_{xx} = -3400 \mu$ strains | $\varepsilon_2 = -4600 \mu$ strains |

207

208 3 Experimental and computation dialogue: Linear bifurcation analysis 209 in a 2D framework

210 A first try to simulate VERTEX test and the wrinkling phenomena is the use of linear models in
211 a 2D plane strain setting subjected to uniaxial compressive loading. Due to the specific
212 geometry of the panel specimen used in the VERTEX bench (see Figure 3), the sandwich
213 section is not uniformly strained in the axial direction: the upper skin is more loaded and is
214 where the wrinkling instability is of interest, whereas the lower skin carries a lower
215 compressive load due to the overall bending of the specimen. Therefore, it is assumed that
216 the experimentally measured wrinkling pertains to a one-sided mode. Thus, the thickness of
217 the core in the analytical models is chosen to be 50mm, instead of 20mm (the thickness of the
218 VERTEX sandwich specimens), in order to prevent any interactions between the two skins and
219 being comparable to a one-sided mode. Moreover, the same layup is attributed to both skins
220 (symmetric sandwich section) and the skins' thickness and layup is taken to correspond to the
221 upper skin of the VERTEX sandwich panel (Table 1). Finally, since the load introduction is not
222 as simple, it appears more meaningful to compare critical strains of the upper skin rather than
223 critical loads, which also allows a direct comparison with the experimental results reported in
224 Table 2.

225 3.1 Analytical formulations

226 A number of analytical wrinkling formulae are considered to evaluate the critical bifurcation
227 load in the two-dimensional, plane strain setting, see also (Ginot et al., 2021). In many cases,
228 the skin stiffness appearing in the formula is expressed by the longitudinal Young's modulus.
229 Since composite laminated skins are studied, this property is computed from the flexural

230 rigidity in the direction of the compressive load as $E_{s\ flex} = \frac{12}{D_{11}^* t_s^3}$ (D^* is the inverse of the
231 bending stiffness matrix of the laminate). We refer to the original works for the details of the
232 models taken from the literature: (Hoff and Mautner, 1945; Niu and Talreja, 1999; Leotoing,
233 2001; Douville and Le Grogneq, 2013). Note that, for Hoff and Mautner’s pioneering formula:
234 $\sigma_{crit} = Q(E_{s\ flex}E_cG_c)^{1/3}$, where E_c and G_c are the core modulus and the core transverse
235 shear modulus, respectively, Q is a constant that has been theoretically calculated at 0.91, but
236 Hoff and Mautner recommend a “practical” constant Q of 0.5 considering that Q plays the
237 role of a knock down factor. Both values are compared with test results.

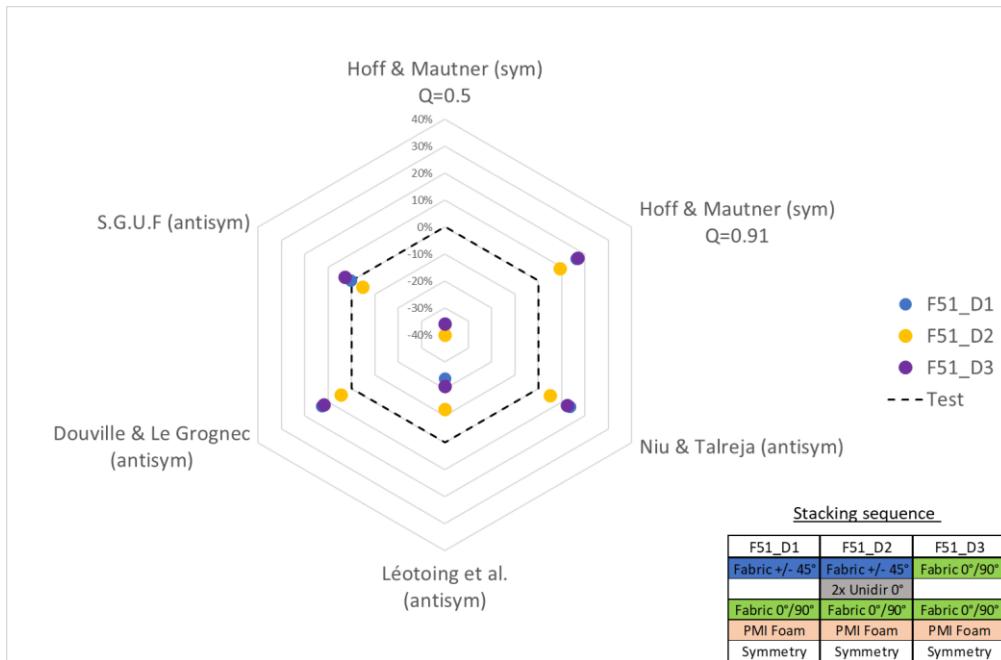
238 As in (Ginot et al., 2021), new results obtained by a S.G.U.F. model are also reported. In order
239 to refrain from simplifying assumptions that may introduce theory-driven inaccuracies, a high-
240 order kinematics with through-thickness cubic axial displacement and quadratic transverse
241 displacement is used for the composite skins. So, parabolic transverse shear strains as well as
242 a linear thickness-stretch are retained. The model for the core is quasi-3D with the
243 displacements approximated by through-thickness polynomials of 12th order. The initial stress
244 matrix is computed upon uniformly straining the whole sandwich section (i.e., the core carries
245 a certain amount of initial compressive load also) and by referring to von Kármán non-
246 linearities. A Navier-type solution is adopted for defining the longitudinal periodic pattern,
247 see, e.g., (D’Ottavio and Polit, 2015; D’Ottavio et al., 2016). Since the wavelength of the
248 wrinkling pattern is an input, the actual wrinkling strain is obtained from the minimum
249 eigenvalue among all processed wavelength responses.

250 For the specimen F51_D3 tested in shear, an equivalent uniaxial model is formulated as
251 suggested by Plantema (1966) and Kassapoglou (2010): assuming that the principal

252 compression load occurs at 45° (pure shear), the analytical formulations for wrinkling are used
253 upon “rotating” the relevant quantities in the direction of the applied compression. Here, for
254 skins composed of $\pm 45^\circ$ fabrics, this is equivalent to switching to $0^\circ/90^\circ$ fabrics (see the
255 stacking sequence in Figure 8). It is worth noticing that this approach is expected to be
256 conservative as much as a certain stabilising effect introduced by the tensile load in the
257 direction perpendicular to the compression axis is neglected in the present plane strain
258 setting.

259 3.2 Radar comparison graph

260 The results of the considered models are presented in the radar comparison graph of Figure 8
261 in terms of relative percentage differences between the analytical wrinkling strains and the
262 mean strains at specimen failure (given in Table 2). The dotted line indicates perfect
263 correlation with the tests. A positive percentage shows an optimistic model, a negative
264 percentage shows a conservative model. **The wrinkling strain of analytical models are**
265 **obtained from the corresponding** load or stress through the equivalent membrane rigidity of
266 the skin. The minimum critical wrinkling strain between symmetric and antisymmetric
267 wrinkling modes is chosen for analysis.



268

269

Figure 8: Radar comparison graph between linear models and VERTEX test results.

270

It is first noticed that the correlation for the specimen F51_D3 is of the same order as for the specimens tested mainly in compression. This confirms that the approach of taking only the compression component seems consistent, even if the specimen is not purely loaded in shear (principal compressive direction at 38°, see § 2.4).

274

The results show that the models of Douville and Le Grogneac, Niu and Talreja and Hoff and Mautner (with $Q = 0.91$) are optimistic while those of Hoff and Mautner's with the knock-down factor $Q = 0.5$ and of Léotoing et al. provide conservative predictions. The quasi-3D analytical S.G.U.F model performs remarkably well for all configurations, yielding at most errors of about 5% on the conservative side. There are many reasons for the analytical expressions to deviate from the experimental measurements. In general, the models from the literature studied here rely on various *ad-hoc* assumptions that can produce a certain inaccuracy depending on the considered problem.

281

282 The core model **is attributed a major** role in the discrepancy between the computed and
283 experimental buckling loads. All analytical models (including the S.G.U.F model) adopt a
284 constant linear elastic behaviour; **in addition, the models by Niu and Talreja and Douville and**
285 **Le Grogneec rely on the assumption of an isotropic core. In reality, the PMI foam is slightly**
286 **anisotropic (Young’s modulus E , tangential modulus G and Poisson’s ratio ν are not related**
287 **by Lamé’s formula $G = \frac{E}{2(1+\nu)}$) and it** has different properties in tension and compression (see
288 next § 4.4). In the analytical models, however, the modulus has been taken equal to the simple
289 average between tension and compression. Niu and Talreja (1999) have shown that
290 **transverse** shear effects can be important with short wavelengths. Léotoing et al.’s model
291 shows conservative correlations with the tests, **but** the discrepancy with the other models
292 raises questions: **it is worth recalling that** this model **discards the core’s axial stiffness** (“anti-
293 plane core”) and **postulates** a simplistic distribution of the shear stress **along** the core
294 thickness.

295 Further, questions may be asked about the **definition of an equivalent Young’s modulus of**
296 **the** composite laminate skin modelling **that neglects the** membrane/bending coupling terms
297 (matrix B) for specimens F51_D1 and F51_D2,. However, it is worth recalling that the
298 benchmark (Ginot et al., 2021) has shown that, for this type of stacking (similar thickness and
299 stiffness), this coupling is not of major importance in the critical buckling load and should
300 hence not justify such differences in correlations.

301 Finally, the considered analytical bifurcation buckling formulae do not consider any type of
302 initial imperfection, which is known to be a major reason for excessively optimistic failure
303 loads (Ley et al., 1999; Fagerberg and Zenkert, 2005b). Despite the doubtless attractiveness of

304 such formulae in terms of required computational effort, this drawback questions their
305 applicability for a reliable sizing. So, analytical wrinkling analysis has been enhanced towards
306 initial imperfections in (Kassapoglou et al., 1995; Fagerberg and Zenkert, 2005b). However, its
307 use in pre-design phases may pose difficulties since specific equipment (as DIC) may be
308 required for identifying imperfection amplitudes. Therefore, the classical knock-down factor
309 approach is widely adopted for artificially reducing the theoretical bifurcation loads, as
310 promoted by the early work of Hoff and Mautner. Their **knock-down** coefficient $Q = 0.5$
311 provides indeed conservative loads in all configurations tested, but it may lead to excessive
312 margins of safety that are detrimental for an optimal lightweight structure.

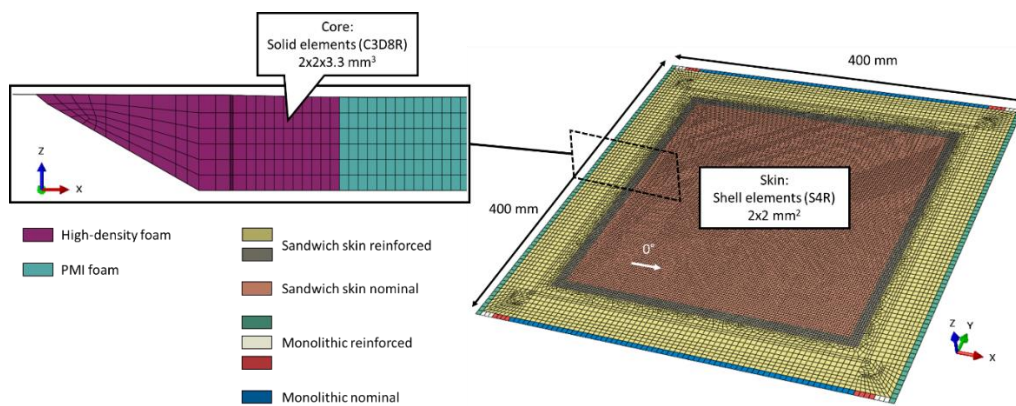
313 Imperfection sensitivity is known to play a relevant role in presence of equilibrium paths with
314 an unstable post-buckling response. This is precisely the case of sandwich wrinkling because,
315 as experimentally observed, the weak core undergoes compressive or tensile failure as soon
316 as local skin indentation occurs. Since slight initial dents have been observed by SDIC at the
317 upper skin (see (Ginot et al., 2023) for more details), **the modeling strategy aims to follow**
318 **the non-linear response including some material and geometrical non-linearities up to**
319 **failure**. This is the objective of the following sections, in which the experimental-numerical
320 dialogue is extended towards a non-linear FEM accounting for the real initial geometry of the
321 tested panels.

322 4 Development of a non-linear finite elements panel model

323 4.1 3D FE panel model definition

324 The geometry of the sandwich specimen panels, with the integration of the reinforcements
325 (core and skins) around the nominal area (Figure 9) is taken into account in this model. The

326 monolithic area bolted to the VERTEX test bench is not represented, just a 5 mm wide strip
 327 remains: The area modelled by the FEM is thus 400 x 400 mm². ABAQUS S4R elements are
 328 used for the skin and monolithic parts and ABAQUS C3D8R elements are used for the core of
 329 the sandwich. The skins and the core are assumed to be perfectly bonded and, therefore, they
 330 are linked by coincident nodes. Léotoing et al. (2002) recommend a minimum of 4-5 elements
 331 per wrinkling half wavelength. The measured wrinkling half wavelengths in the specimens are
 332 about 8 mm to 10 mm depending on the sandwich configuration. The horizontal element size
 333 is then set to 2 mm in the nominal area. The total number of degrees of freedom is around
 334 720000 for the whole model. The computation is performed using dynamic analysis with
 335 ABAQUS Explicit. The choice of this analysis is explained in § 4.4.2.

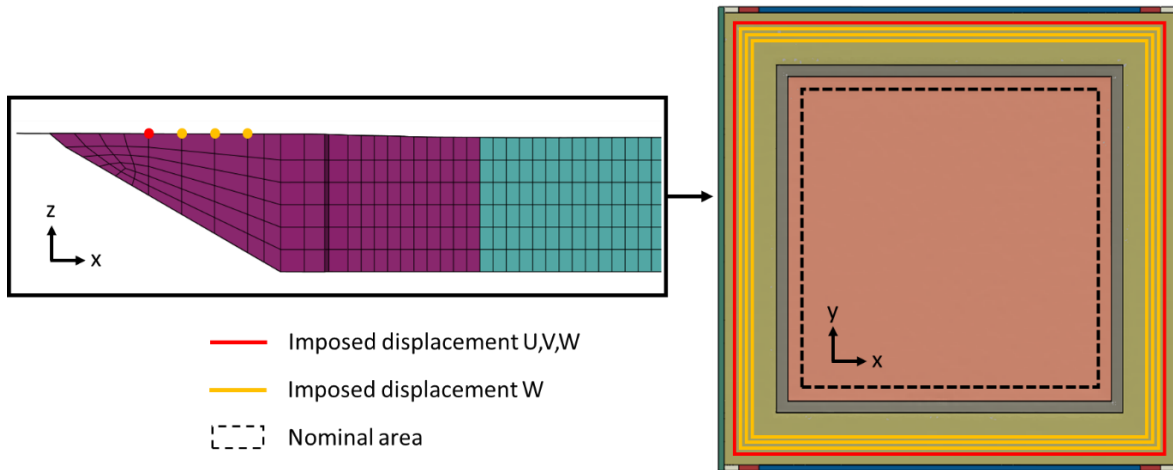


336
 337 *Figure 9: FE panel model definition.*

338 4.2 Boundary conditions imposed by the displacements measured by SDIC

339 **In order to avoid excessively idealized boundary and loading conditions, and in absence of**
 340 **a transfer function explicitly linking the actuator forces of the VERTEX bench to the load**
 341 **acting on the specimen,** Stereo Digital Image Correlation (SDIC) data are extracted and used
 342 to apply a loading path in the numerical model. This approach has been successfully developed
 343 and used for the previous experimental and computation dialogues on VERTEX test campaigns

344 (Serra et al., 2017a; Trellu et al., 2020). It consists of imposing the displacements (U,V,W)
345 measured by SDIC on a rectangular frame of upper face nodes (red in Figure 10), plus out-of-
346 plane displacements (W) on 3 additional rectangular frames (orange in Figure 10).



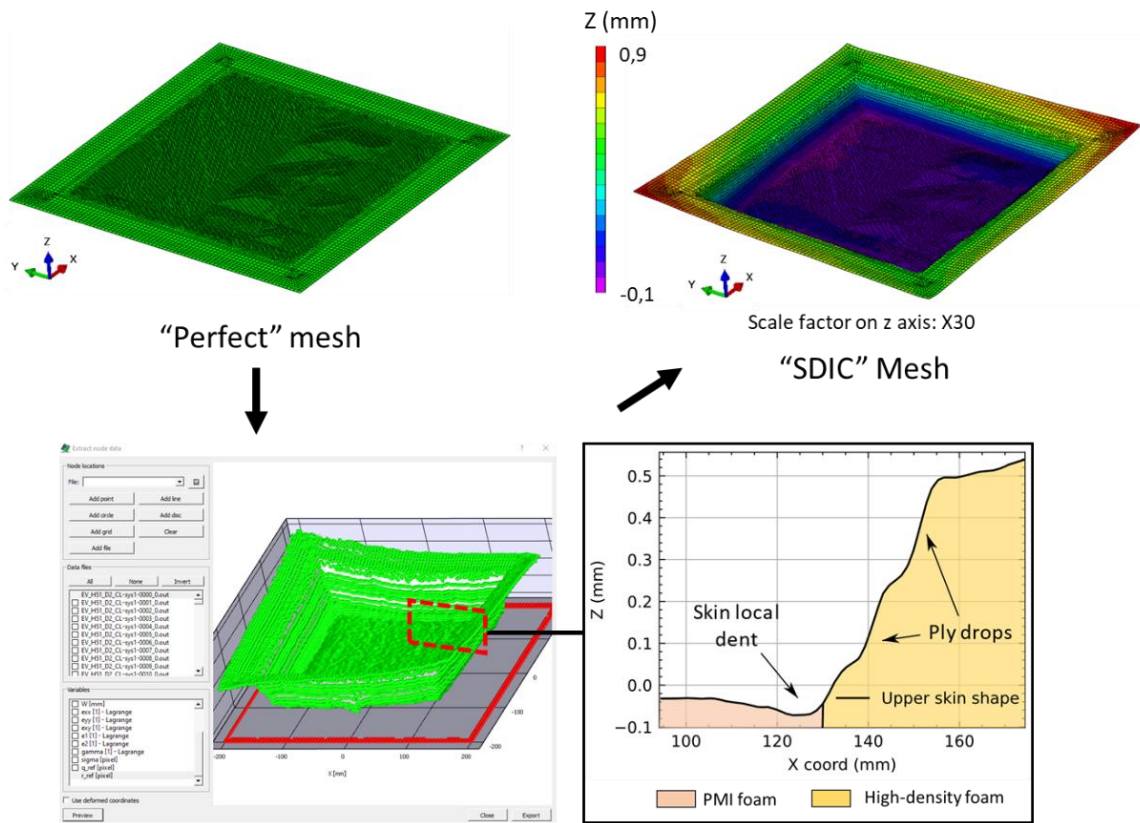
347
348 *Figure 10: SDIC loading condition imposed in the FEM by four imposed displacement frames.*
349 Rotations are then introduced by the out-of-plane displacement gradient between the loading
350 frames (Sztefek and Olsson, 2008). Displacements are implemented in the model as
351 amplitudes against time and are linearly interpolated between two successive SDIC
352 measurements to represent their evolution during the test.

353 4.3 Initial imperfections

354 4.3.1 Mesh building based on SDIC data

355 The introduction of measured imperfections from a real part in a finite element analysis has
356 been strongly studied in the Thin-Walled Structures community. The most commonly used
357 method to approximate geometrical imperfections is using a double Fourier series (Arbocz,
358 1982). In addition, this formulation allows the Fourier coefficients to be random variables for
359 probabilistic analysis (Wagner et al., 2020). Recently, the use of double Fourier for mesh
360 generation based on SDIC data was performed to model the effects of geometric

361 imperfections on the buckling behaviour of woven composite cylindrical shell structures (Xin
362 et al., 2022). In our case, generating imperfections through a double Fourier series is not used.
363 Fourier series such as a sum of periodic sine function would not **correctly** represent the ply
364 drops offset, present in the sandwich skins between nominal and reinforced **areas**, because
365 ply drops are not periodic. Another method is to use SDIC measurements of the initial
366 specimen profile and apply them directly to generate a mesh. This method has already been
367 used on CFRP panels under compression (Featherston et al., 2012). A perfect mesh is first
368 made. Then, the out-of-plane positions, z , are extracted from SDIC data at the corresponding
369 x and y positions of the upper skin nodes of the perfect mesh (Figure 11). In nodes at the FEM
370 boundaries, where SDIC data are not consistent or available (SDIC measuring window edges),
371 linear extrapolation from the nearest measured data points is used. The “SDIC” mesh has
372 shown that very small ripples can trigger wrinkling localisation. It is necessary to dissociate the
373 ripples due to the measurement uncertainty from the actual imperfections. The parameters
374 used for the SDIC are recommended by the DIC software to minimise data noises from the
375 image characteristics (resolution, contrast, etc.); Subset size is 35 px; step size is 15 px; with a
376 pixel size equal to 0.2 mm. With these parameters, the average confidence margin of the
377 measurements is about 0.01 pixel, which is equal to 0.002 mm. The imperfections present in
378 the specimens were measured at about 0.04 mm in out-of-plane direction z , which is an order
379 of magnitude greater than the SDIC confidence margin.

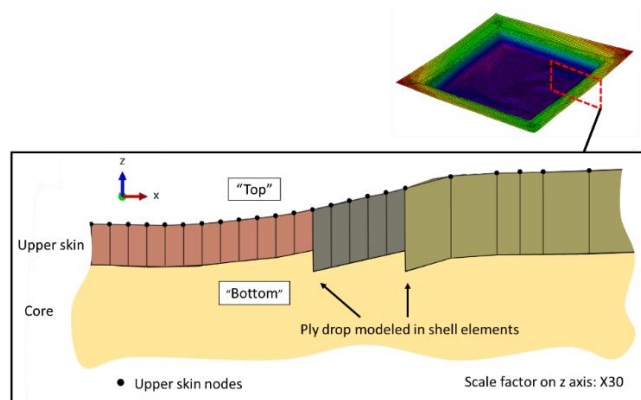


Out-of-plane coordinate z extraction from SDIC data at zero load

380

381 *Figure 11: Upper sandwich face mesh construction from measured SDIC out of plane*
 382 *coordinates z.*

383 Note that the measured surface is the upper face of the skin, the ply drop offsets are
 384 integrated into the "SDIC" mesh. The thickness offset in the shell elements of the upper skin
 385 is then set to "top" (Figure 12).



386

387 *Figure 12: Thickness offset modelled in the shell elements of the upper surface in the "SDIC"*
 388 *mesh.*

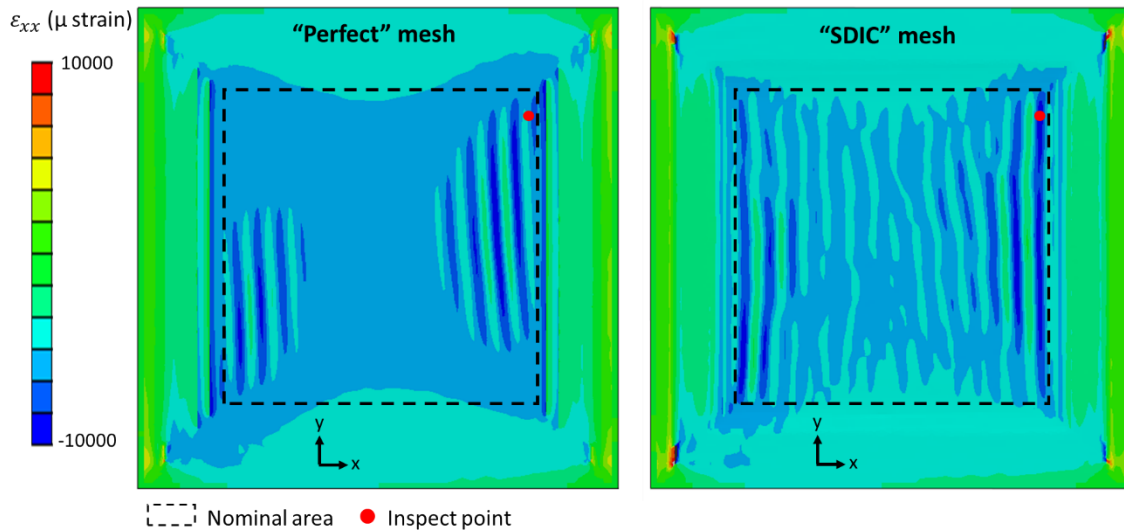
389 4.3.2 Effects of defects

390 Figure 13 illustrates the influence of the initial imperfections introduced into the mesh on in-
391 plane and out-of-plane strain. By comparing the results from a perfect mesh (left image in
392 Figure 13 (a)) and those from the “SDIC” mesh with imperfections (right image in Figure 13
393 (a)), we observe:

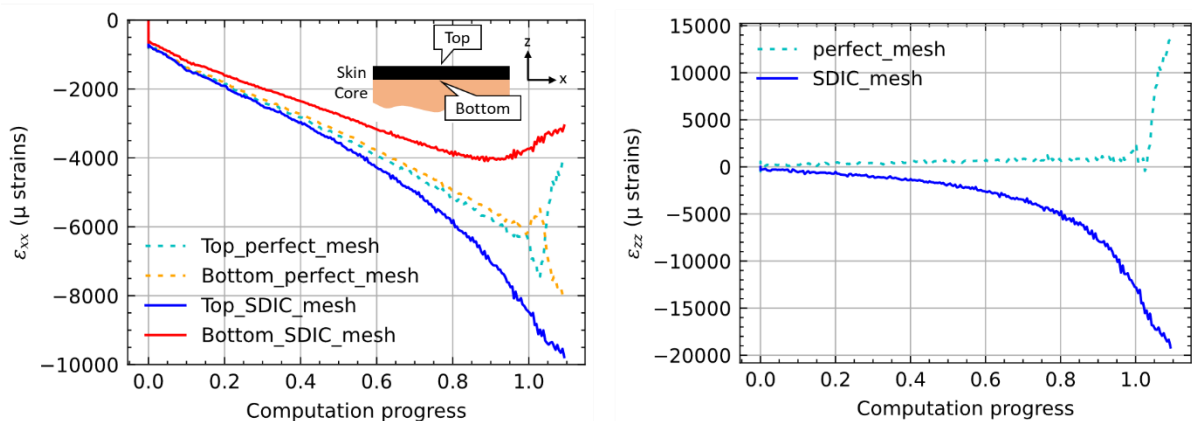
394 (1) In Figure 13 (a), wrinkling waves are represented by blue areas with high strain gradients
395 induced by the local bending of the wrinkling waves. In the perfect mesh, the wrinkling pattern
396 is smooth and straight, whereas in the “SDIC” mesh it is less regular and follows the
397 localisation and the geometry of the initial imperfections. **The dissymmetry of the wrinkling**
398 **zone displayed in the “perfect mesh” results is induced by the loading which is a pure**
399 **compressive loading along X axis (Table 2). This dissymmetry appears slightly less pronounced**
400 **in the “SDIC mesh” results. This difference is likely to be due to the non-constant top surface**
401 **level (z-position due to the geometric imperfections)**

402 (2) Figure 13 (b) is the plot of strain evolution of the top and bottom faces in the upper skin of
403 the sandwich at the inspection point (red point in Figure 13 (a)). The Initial imperfections in
404 the “SDIC” mesh induce local bending effects. This is shown by the difference in the in-plane
405 strain evolution between the top and bottom faces (solid lines in Figure 13 (b)). The evolution
406 rapidly becomes non-linear and the buckling onset is characterised by a progressive growth of
407 the non-linearity. In contrast, in the perfect mesh (dotted line in Figure 13 (b)), the strain
408 difference between the top and bottom faces is almost zero and linear until the bifurcation
409 (computation progress equals 1). These local bending effects generate high out-of-plane
410 strains in the core (Figure 13 (c)) from the beginning of the loading. **Due to the low mechanical**
411 **performances of the PMI foam, the out-of-plane** strength can be reached rapidly and trigger

412 the core to fail. Consequently, a **more accurate** modelling of the core is proposed in the next
 413 **subsection.**



(a) Strain ϵ_{xx} field on top face of the sandwich's upper skin at computation progress equal to 1 for "perfect" and "SDIC" meshes.



(b) ϵ_{xx} at inspect point on top and bottom faces against computation progress for "perfect" and "SDIC" meshes.

(c) ϵ_{zz} at inspect point in core against computation progress for "perfect" and "SDIC" meshes.

414

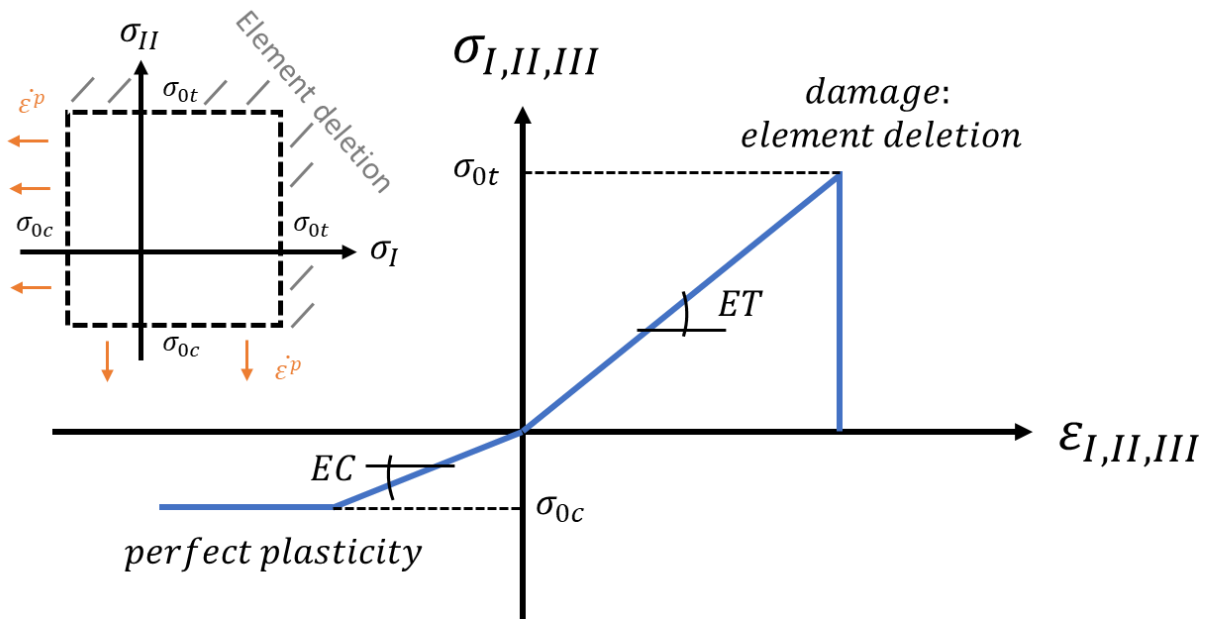
415 *Figure 13: FE results of "Perfect" and "SDIC" meshes from the loading condition of specimen*
 416 *F51_D1 (axial compression)."*

417 4.4 Core behaviour modeling

418 4.4.1 Constitutive law for the core

419 PMI foam exhibits different mechanical behaviours in compression and tension. In
 420 compression, the foam behaves like a ductile material where an elastic response is first

421 observed, followed by a plateau corresponding to the buckling of the cell walls and then the
422 cell walls interact, increasing the overall stiffness of the foam (called densification). In tension,
423 the behaviour is rather fragile, with brittle failure. In our case, the difference in mechanical
424 characteristics between compression and tension is significant, with the tension modulus and
425 strength being more than twice the compression ones. **Abrate (2008) shows that hydrostatic
426 pressure has an important effect on foam failure. Since the anisotropy in the elastic regime
427 is not very important (Wang et al., 2010), an isotropic bi-modulus constitutive law is
428 assumed and implemented in the principal directions. In compression, a perfect
429 elastoplastic model is used. The foam densification is not modelled here, because it appears
430 for very large strains not reached in our experiments. In tension, an elastic response is used
431 with damage modelled by element deletion (Figure 14). Note that a yield surface with a
432 crushable foam model is available in ABAQUS software, but it does not provide the
433 possibility of working with bi-modulus behaviour. In compression, experimental results
434 indicate that the compressive strength is limited by the buckling of the cell walls and show
435 that it can be closely approximated by a maximum principal stress criterion (Gibson and
436 Ashby, 1997). So, a maximum principal stress criterion is chosen as the yield surface in
437 compression and tension (Figure 14). This greatly simplifies the integration of plastic strains
438 $\dot{\varepsilon}^p$ which are classically taken normal to the yield surface. An elliptical yield surface such as
439 described by Deshpande and Fleck (2000) or Huo et al. (2022) would introduce a more
440 complex calculation.**



441

442 *Figure 14: Constitutive law and yield surface of the PMI foam core used in the FE panel*
 443 *model. Parameters ET ; EC ; σ_{0c} ; σ_{0t} are calibrated from characterisation test campaigns in*
 444 *traction (ASTM C297 (ASTM C297, 2004)) and compression (ASTM C365 (ASTM C365, 2011)).*

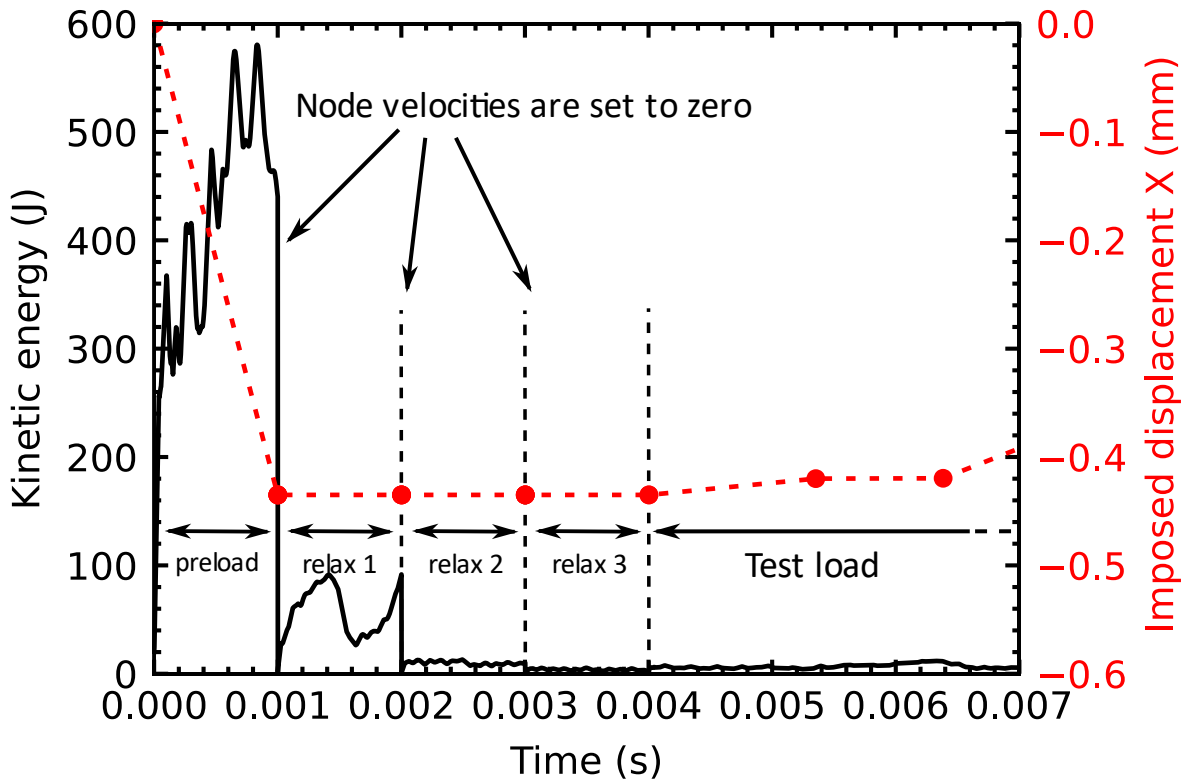
445 4.4.2 Explicit computation

446 The constitutive law of the foam was first implemented with implicit computations using
 447 ABAQUS UMAT. However, **the resulting elasto-plastic instability problem** led to difficult
 448 convergence problems, a difficulty also noticed by Leotoing (2001). The post-buckling
 449 behaviour was not reached in implicit computation. The choice of dynamic explicit
 450 computation was therefore made, and the constitutive law was implemented with ABAQUS
 451 VUMAT. The explicit solver can be relevant for quasi-static computations when these are
 452 subject to convergence problems (significant non-linearity, complex contact management). In
 453 the case of buckling, the explicit analysis allows the highly nonlinear post-buckling structural
 454 response to be followed (Bisagni, 2000). The use of an explicit solver for the solution of a quasi-
 455 static problem has some particularities that have to be dealt with (Pinho, 2005; Serra et al.,
 456 2016). Relatively to a standard implicit solver, an explicit solver needs very small increments
 457 (depending on the size of the element). Thus, analysis usually requires a large number of

458 increments, and a considerable numerical displacement speed compared to the actual quasi-
459 static problem. Kinetic energy is then introduced, and a damping system is needed to reduce
460 the dynamic vibration. During these steps, a numerical error can accumulate, and the work of
461 external forces can be converted into energy other than the internal energy, such as kinetic
462 energy, hourglass control energy and damping energy. It must be checked that additional
463 energy is kept at a negligible level by selecting the right numerical displacement speed while
464 keeping a reasonable calculation time. The numerical displacement speed taken is 100 mm/s
465 with a time increment of 10^{-7} s. On the other hand, increasing the stable time increment
466 prevents unwanted vibrating effects. The ABAQUS function "*MASS SCALING" (Abaqus
467 Analysis user's Manual) was used to artificially increase the mass of the model. To ensure that
468 changes in the mass and consequent increases in the inertial forces did not alter the solution
469 significantly, a calculation was performed with a numerical displacement speed that was a
470 quarter of the initial one and showed similar results.

471 In the test process, residual strains are induced in the specimen when it is bolted onto the
472 VERTEX test bench (see detail in (Ginot et al., 2023)). This is transcribed in the FEM's loading
473 conditions with a preload imposed by large displacements in the four displacement frames
474 (Figure 10). It is necessary to dissipate the kinematic energy introduced by the preload as far
475 as possible. The displacements are too large to be handled by the numerical displacement
476 speed without a significant increase in computation time. The solution shown, in Figure 15, is
477 the simulation of three steps of relaxation after the preload step. In these steps, the velocity
478 of each node of the FEM is set to zero to keep the kinematic energy at zero, then left free so
479 that the panel can take its distorted equilibrium form. During these relaxation steps, the
480 imposed displacements are kept constant (the red dotted line in Figure 15 is the average

481 displacement X of the left side of the first displacement frame in Figure 10). The test loading
 482 conditions are then introduced. This solution has already been used to dissipate energy after
 483 impact in (Serra et al., 2021).

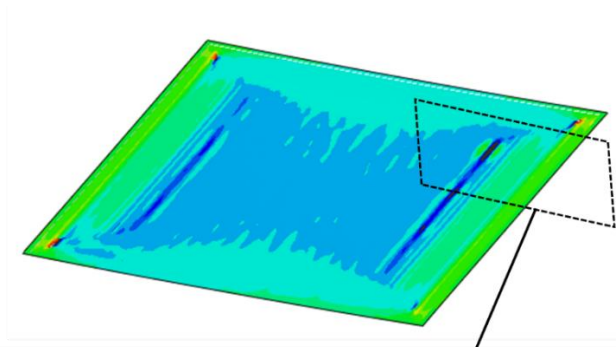


484
 485 *Figure 15: Overall kinematic energy versus time in FEM from the loading condition of*
 486 *specimen F51_D1. 3 relaxation steps allow kinetic energy dissipation from large*
 487 *displacements in preload step.*


488 4.4.3 Effects of the compressive elastoplastic and tensile damage core behaviour

489 The study of the core non-linear behaviour in the local instability is not completely original. In
 490 the literature, several authors have tried to add this parameter to their numerical models but
 491 have remained at the beam scale. Stiftinger and Rammerstorfer (1997) included a core
 492 crushing behaviour in a sandwich beam FEM and reported a slight decrease of the maximum
 493 load and a sudden drop in the load. Léotoing et al. (2002) used a perfect **elastoplastic** model
 494 with a von Mises yield function, where the constitutive law is calibrated from a uniaxial

495 compression test. They noted that the plastic strains are located where wrinkling occurs. The
496 transition from the elastic to the plastic state was immediately followed by a drastic decrease
497 in the overall stiffness of the sandwich beam **In our built-up structure, inclusion of the**
498 **compressive elastoplastic and tensile damage behavior of the core allows to reproduce the**
499 **observed failure scenario.** Firstly, plastic strains develop locally at the skin interface, then,
500 large out-of-plane strains make the core fail in tension (Figure 16).



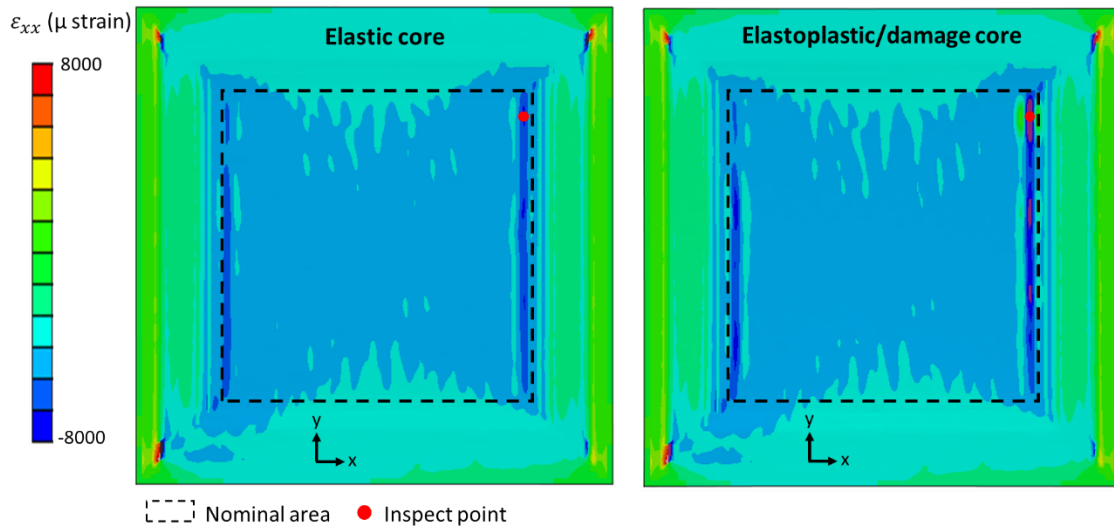
| Computation process | Local cross section | |
|---|---------------------|-------------------|
| | PMI foam | High-density foam |
| 90% | | |
| 95% | | |
| 98% | | |
| 99.5% | | |
| 100% Tensile failure (elements deleted) | | |

 Plastic strains in solid elements

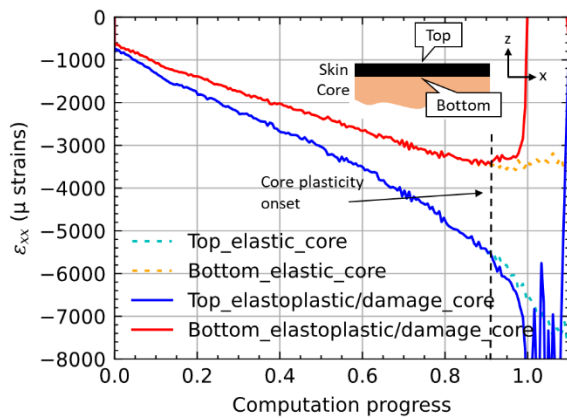
501

502 *Figure 16: FEM cross sections with elastoplastic+damage constitutive law for the core. Plastic*

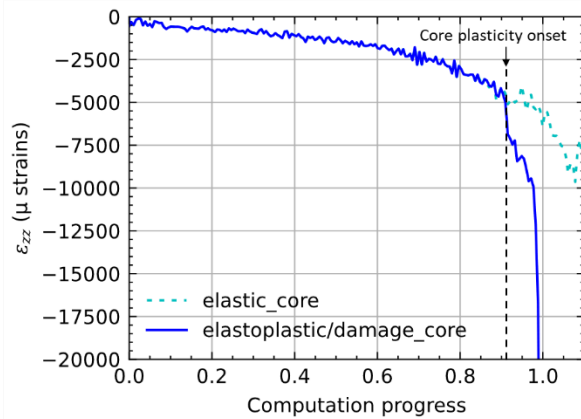
503 *strains develop locally, then the core fails in tension (modelled by element deletion).*



(a) Strain ϵ_{xx} field on upper skin of top face of the sandwich at computation progress equal to 1 for elastic and elastoplastic+damage core modeling.



(b) ϵ_{xx} at inspect point on top and bottom faces against computation progress for elastic and elastoplastic+damage core modeling.



(c) ϵ_{zz} at inspect point in core against computation progress for elastic and elastoplastic+damage core modeling.

504

505 *Figure 17: FE results of elastic and elastoplastic+damage core modelling from loading*
 506 *condition of specimen F51_D1 (compression). The constitutive law introduces an elastoplastic*
 507 *behaviour in compression and an elastic response with damage modelled by element*
 508 *deletion in tension (see Figure 14).*

509 Figure 17 illustrates the results of a comparison between a bi-modulus full elastic core
 510 behaviour (left image in Figure 17 (a)) and one with the elastoplastic and damage behaviour
 511 of the core added (right image in Figure 17 (a)). The transition from an elastic to a plastic state
 512 tends to develop non-linear, in-plane strains (solid line in Figure 17 (b)) and out-of-plane
 513 strains (solid line in Figure 17 (c)), which increase rapidly with loads. The plastic state develops
 514 locally in the panel under the wrinkling waves with maximum amplitude, magnifying the non-

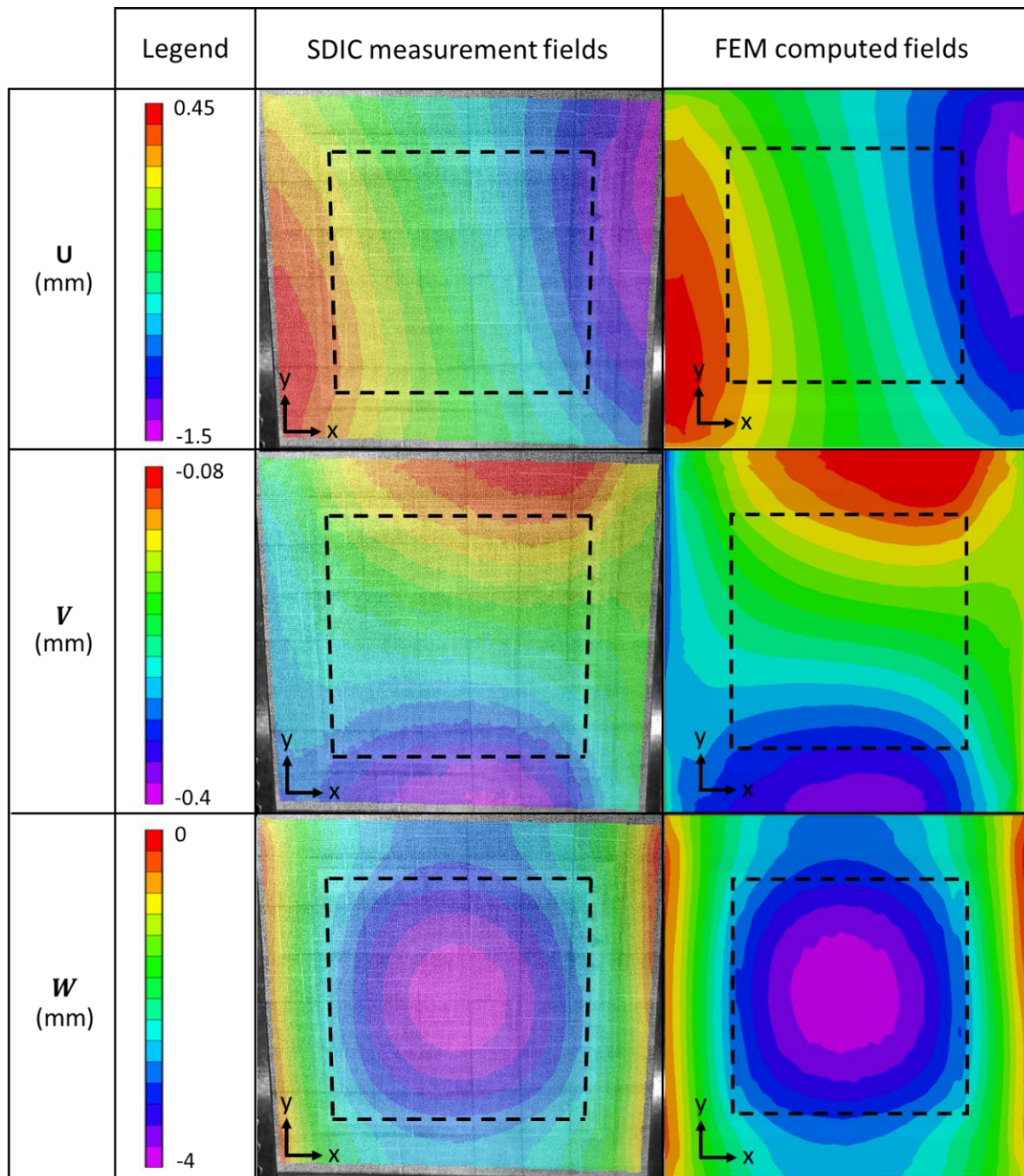
515 linearity and localising the wrinkling failure (purple area in Figure 17 (a) right image). **The jump**
516 **observed in (Figure 17 (b) and (c)) at the onset of plasticity is due to the implemented**
517 **perfectly elastoplastic behaviour.** The integration of the elastoplastic and damage behaviour
518 of the core makes the panel fail brusquely (considering when the first tensile failure of the
519 core occurs with the computation progress equal to 1), whereas, in the case of purely elastic
520 core behaviour, buckling is progressive and buckling onset is not easy to interpret.

521 5 Non-linear finite element model of panel: Experimental and 522 computation dialogue

523 5.1 Specimens under compression

524 5.1.1 Overall behaviour

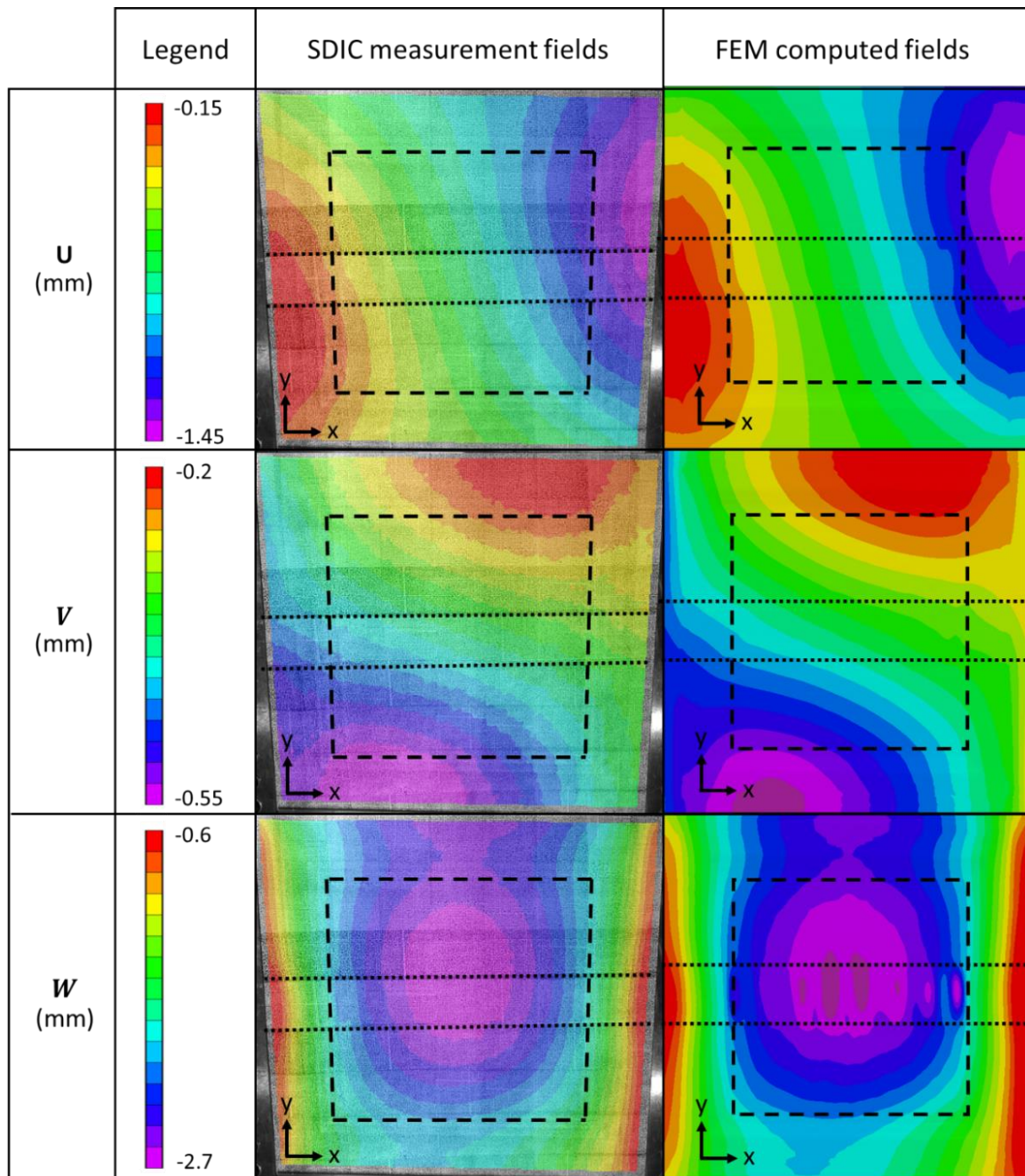
525 Figure 18 and Figure 19 show the displacement fields in the upper face for specimens F51_D1
526 and F51_D2 obtained by SDIC versus those computed by the FEM. Good agreement is found
527 between experimental and numerical displacement fields. **In-plane** and out-of-plane
528 displacement fields computed by FEM are similar to those measured in the nominal area. This
529 confirms that the loading condition methodology developed in § 4.2 is effective to introduce
530 the loading path imposed by the VERTEX test bench in the sandwich specimen.

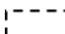



Nominal area

531

532 *Figure 18: Displacement fields: comparison between experimental measurements and FEM*
 533 *results of the upper face of specimen F51_D1 under compressive loading. Frames were taken*
 534 *just before the core failed in tension in the FEM (93% of test progress).*



 Nominal area
 Unidir 0° ply area

535

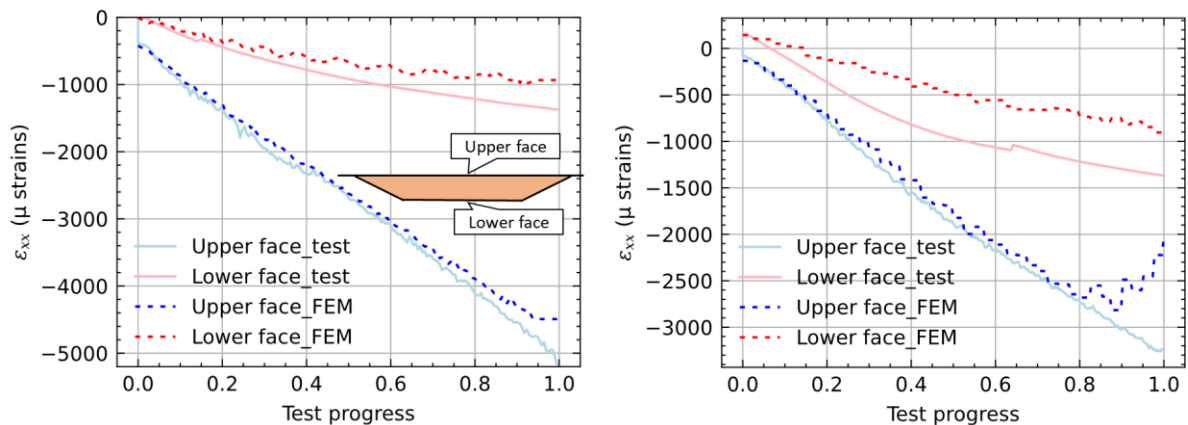
536 *Figure 19: Comparison of displacement fields between experimental measurements and FEM*
537 *results of the upper face of specimen F51_D2 under compressive loading. Frames were taken*
538 *just before test failure (99% of test progress).*

539 The specimen panels bend globally, as a consequence of the asymmetric geometry (see § 2.1,

540 Figure 3 and (Castanié et al., 2002)), and the upper skin is more loaded than the lower skin

541 (Figure 20). The FEM represents the global membrane and bending stiffness of the sandwich

542 panels adequately, as shown by the acceptable correlation in the strain of the upper and the
 543 lower skins in the centre of the panel (Figure 20). This confirms the relevance of the
 544 mechanical and geometrical characteristics used for the simulation. **However, the numerical**
 545 **models are slightly less stiff in bending than either of the specimens, as can be also inferred**
 546 **from the higher values of out-of-plane displacements W in Figure 18 and Figure 19. As a**
 547 **result, the computed compressive strains in the bottom skin are smaller due to the higher**
 548 **tensile load induced by the larger global bending of the panel (Figure 20). As already pointed**
 549 **out by Castanié et al. (2002), the bottom skin of the VERTEX panels is very sensitive to load**
 550 **introduction and local ply drops in the transition region, which can explain the discrepancy.**
 551 **Note that the strains introduced by the assembly of the sandwich panel on the test bench**
 552 **can be seen in Figure 20 and is correctly taken into account in the FEM.**



(a) Strain ϵ_{xx} in the upper and the lower faces centre against test progress for the specimen F51_D1.

(b) Strain ϵ_{xx} in the upper and the lower faces centre against test progress for the specimen F51_D2.

553

554 *Figure 20: Strain ϵ_{xx} in the upper and the lower skins against test progress for specimens*
 555 *F51_D1 and F51_D2.*

556

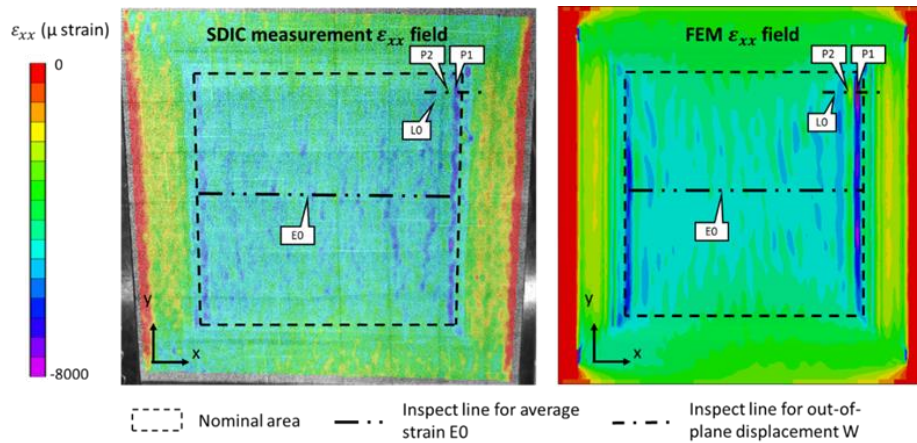
557 5.1.2 Local behaviour

558 In Figure 21 (a) and Figure 22 (a) local gradients in ϵ_{xx} strain fields, represented by deep blue
559 areas in SDIC measurements as well as in the simulation results, are present at the edge of the
560 nominal area.

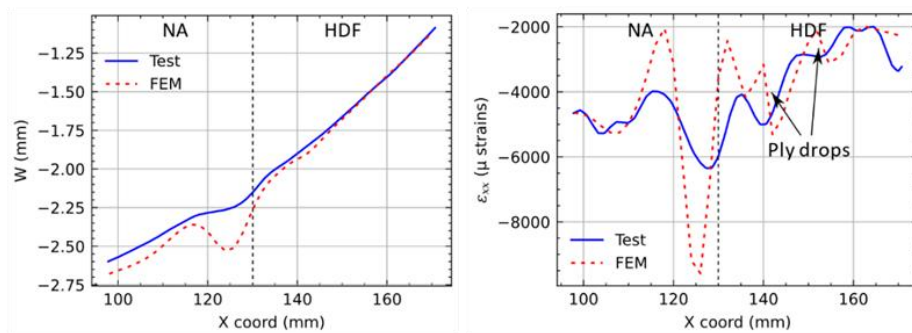
561 This reflects a local bending induced by wrinkles. Wrinkles are shown with the profiles of the
562 curves in Figure 21 (b) and Figure 22 (b) for out-of-plane displacement and in Figure 21 (c) and
563 Figure 22 (c) for strain ϵ_{xx} on inspect line L0 (see Figure 21 (a) and Figure 22 (a)). In Figure 21
564 (d) and Figure 22 (d), the strain evolutions **at inspect points** P1 and P2 are firstly linear with
565 respect to the load and then become non-linear. This is a consequence of the bending effect
566 of the wrinkling wave, which appears at around 80% of the failure load. The strain slopes at
567 P1 and P2 (see Figure 21 (d) and Figure 22 (d)) differ from the averaged one E0. This is due to
568 geometric imperfection generating out-of-plane displacements, which affect local in-plane
569 strains. The difference in slopes and non-linearity at the end of the test, which reflects the
570 onset of buckling, are well represented in the simulations for both specimens. For the
571 specimen F51_D1, the location of the wrinkling predicted by the simulation is consistent with
572 that experimentally observed by SDIC. The profiles of the curves of Figure 21 (b) and (c) show
573 a good match between the test (solid blue lines) and the FEM (dashed red lines), even though
574 larger gradients are present in FEM results. Larger gradients show that the simulation is
575 conservative. Wrinkling is quickly followed by tensile failure of the core, which occurs at 93%
576 of test progress (Figure 21 (b)). At the time studied, i.e. at 93% of the test progress, the local
577 non-linearity resulting from the buckling process is well underway in the simulation whereas,
578 in the test, buckling is just starting to occur. The conservatism of the simulation can be
579 explained by the methodology for introducing imperfections. SDIC measurements of the initial

580 profile's upper face are directly applied to generate the mesh, which implies that the
581 measured curvature is constant over the thickness of the skin. For example, a variation in skin
582 thickness will be simulated as a ripple of the whole skin. It is likely that this method introduces
583 imperfections of greater magnitude than the real ones.

584

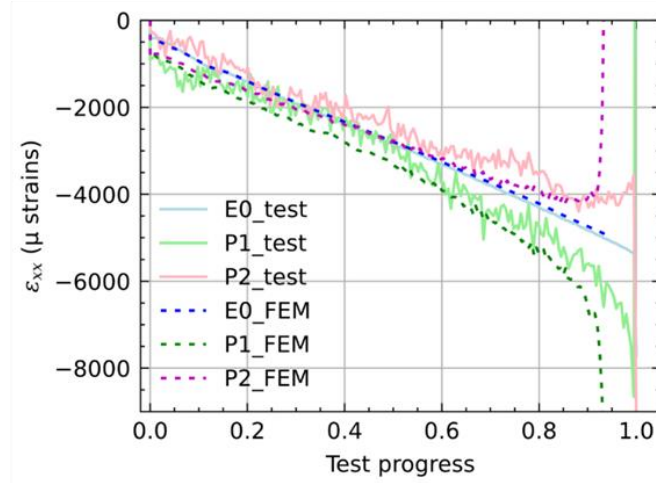


(a) Inspect points and lines on strain ϵ_{xx} field at 93% of test progress.



(b) Out-of-plane displacement on inspect line LO at 93% of test progress. NA=Nominal Area; HDF=High-Density Foam

(c) ϵ_{xx} on inspect line LO at 93% of test progress. NA=Nominal Area; HDF=High-Density Foam



(d) Strain ϵ_{xx} of inspect points P1 and P2 and average strain E0 against test progress.

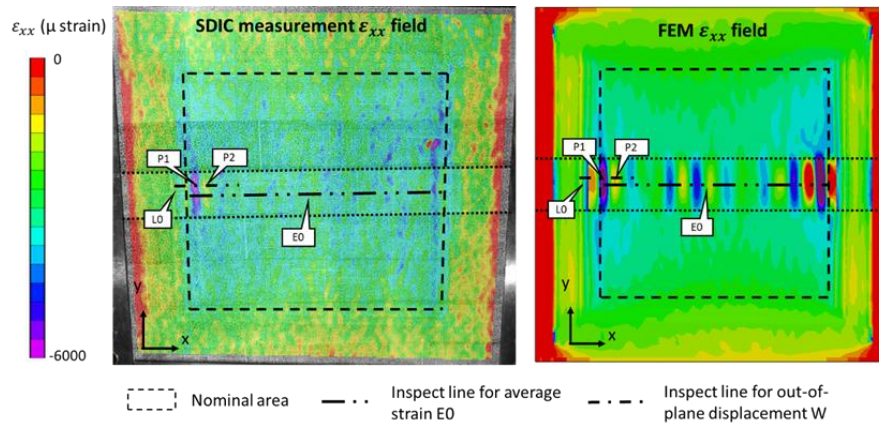
585

586

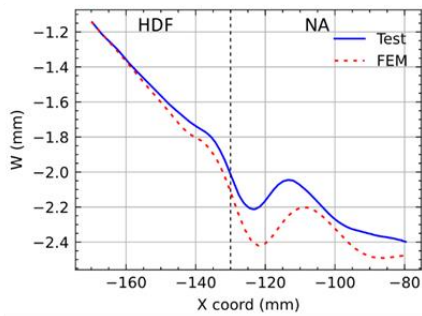
Figure 21: Comparison of fields and curves between test and FEM for specimen F51_D1.

587

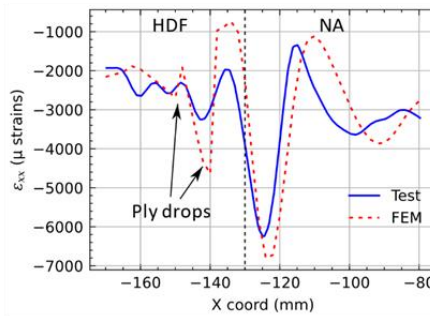
588



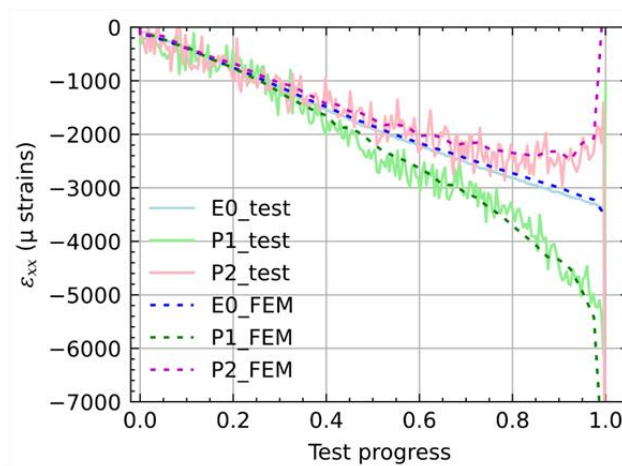
(a) Inspect points and lines on ϵ_{xx} field just before failure.



(b) Out-of-plane displacement on inspect line LO just before failure. NA=Nominal Area; HDF=High-Density Foam



(c) ϵ_{xx} on inspect line LO just before failure. NA=Nominal Area; HDF=High-Density Foam



(d) ϵ_{xx} of inspect points P1 and P2 and average strain E0 against test progress.

589

590 *Figure 22: Comparison of fields and curves between test and FEM for the specimen F51_D2.*

591

592

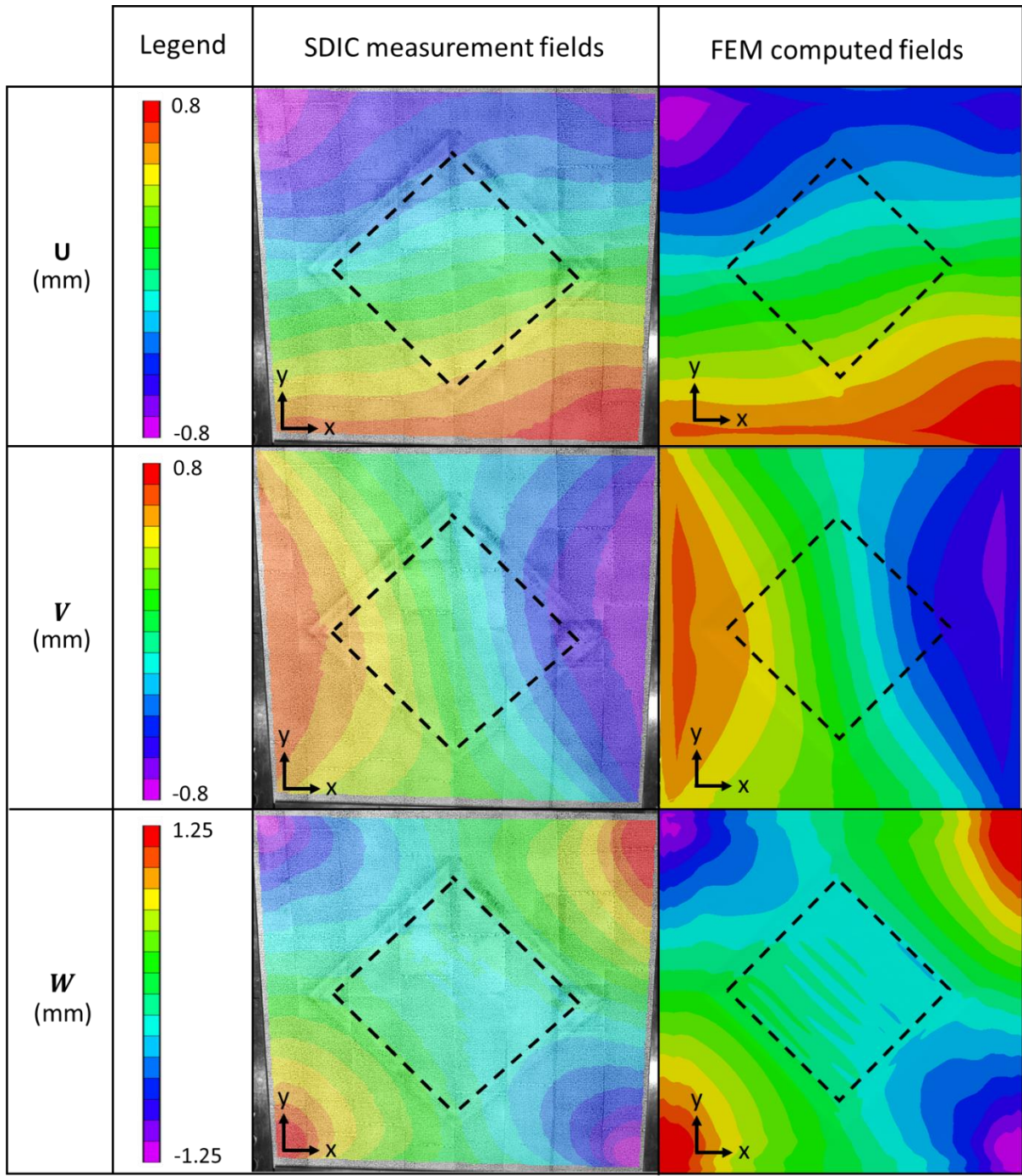
593 For specimen F51_D2, note that a 60 mm wide strip of two Unidir 0° plies is added in the
594 centre of the panel (Figure 22 (a)) and the wrinkling is positioned in this stiffened area, which
595 drains the loads. Several wrinkles appear in the simulation, whereas only one is present in the
596 test (Figure 22 (a)). This might be explained by the fact that the initial geometrical
597 imperfections are less marked here than for specimen F51_D1 (this has already been
598 suggested in section 3) and are not sufficient to localise the buckling to a particular area in the
599 simulation. Nevertheless, a wrinkle is present where wrinkling is observed in the test. The
600 profiles of the curves in Figure 22 (b) and (c) show a very good match between the test (solid
601 blue lines) and the FEM (dashed red lines).

602 5.2 The specimen under shear (F51_D3)

603 5.2.1 Overall behaviour

604 Figure 23 shows the displacement fields measured by SDIC in the upper face of specimen
605 F51_D3 tested under shear loading and enables them to be compared with those computed
606 by the FEM. The comparison is made just before the test failure. Here again, the correlation
607 between experimental and numerical displacement fields is good.

608

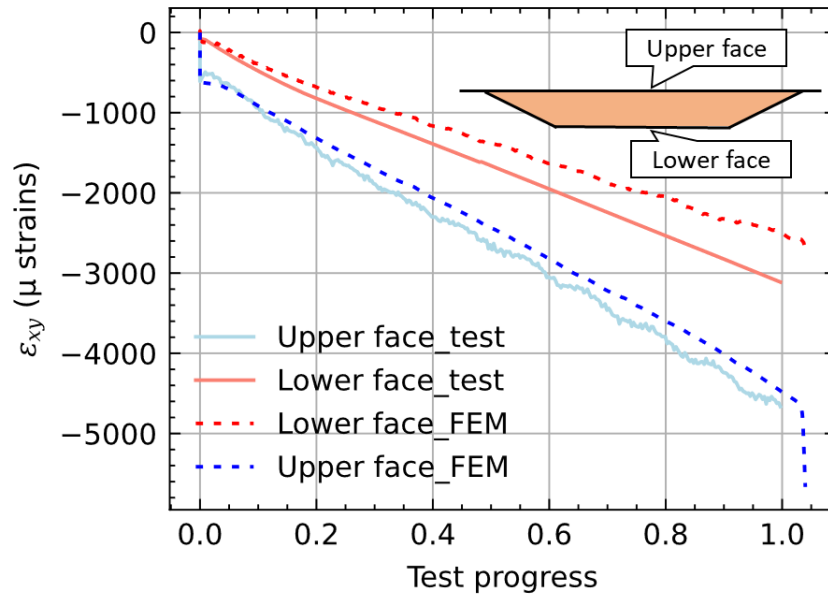


Nominal area

609

610 *Figure 23: Comparison of displacement fields between experimental measurements and FEM*
 611 *results for the upper face of specimen F51_D3 under shear loading. Frames were taken just*
 612 *before test failure (99% of test progress).*

613 The correlation of the shear strain in the upper and the lower faces in the centre of the panel
 614 is acceptable (Figure 24). The FEM represents the global shear stiffness of the sandwich panel
 615 adequately.

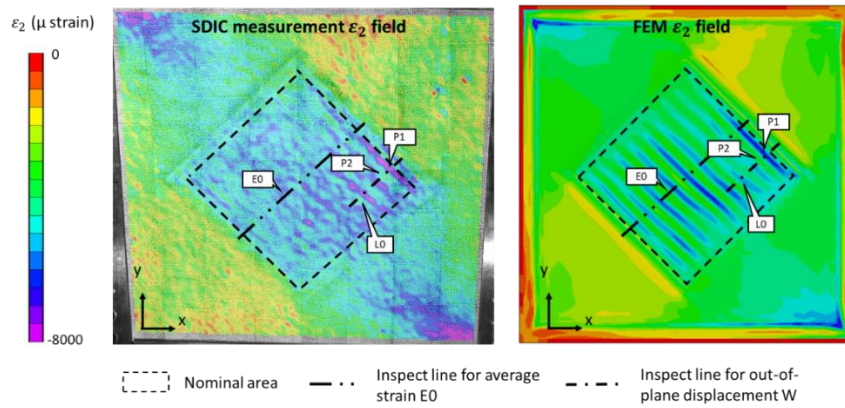


616
 617 *Figure 24: Shear strain ϵ_{xy} of the centre of the upper and the lower faces against test*
 618 *progress.*

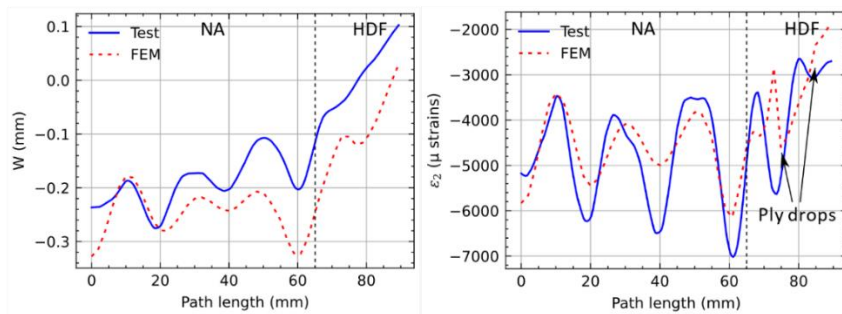
619 5.2.2 Local behaviour

620 Several wrinkles were observed in the nominal area. They are shown in Figure 25 (a) by the
 621 local gradients in principal compressive ϵ_2 strain fields and, in Figure 25 (b) and (c), by out-of-
 622 plane displacement and ϵ_2 strain curve profiles in the wrinkling area. Note that the principal
 623 compressive direction is about 38° from the x-axis, which is why the principal compressive
 624 strain ϵ_2 is expressed instead of the 45° strain, which would be pertinent in pure shear loading.
 625 The simulation is consistent with the localisation of the wrinkles. The observation of several
 626 wrinkling waves allows an accurate determination of the half-wavelength of the buckling
 627 pattern; it is around 10 mm. The simulation is doubly validated by the very good correlation
 628 between (1) the average strain state and (2) the length of the half-wavelength of the buckling

629 pattern. As in the compressive tests, the evolution of the principal compressive strains ϵ_2 at
630 inspect points P1 and P2 shows a linear trend versus loading, followed by a non-linear regime
631 at the end (Figure 25 (d)). Again, this can be attributed to the onset of local buckling that
632 occurred at around 80% of the failure load. The simulation follows the wrinkling phenomenon
633 very well, while being slightly optimistic (Figure 25 (d)).

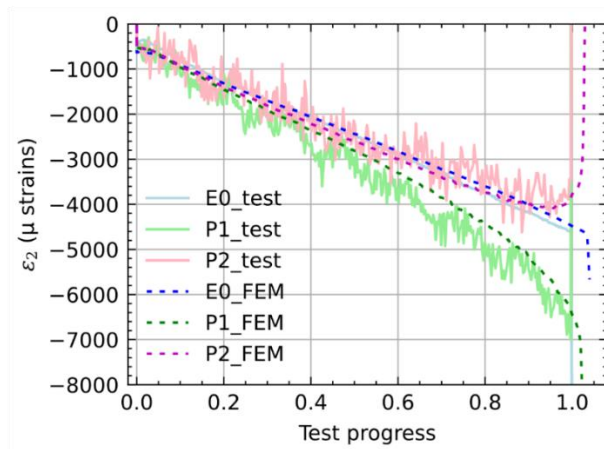


(a) Inspect points and lines on principal compressive strain ϵ_2 field just before failure.



(b) Out-of-plane displacement on inspect line LO just before failure. NA=Nominal Area; HDF=High-Density Foam

(d) ϵ_2 on inspect line LO just before failure. NA=Nominal Area; HDF=High-Density Foam



(e) principal compressive strain ϵ_2 of inspect points P1 and P2 and average strain E0 against test progress.

634

635 *Figure 25: Fields and curves comparison between test and FEM for the specimen F51_D3.*

636 5.3 Radar comparison graph

637 In this section, the radar comparison graph shown in § 3.2 is reused with the results from the

638 non-linear FEM.

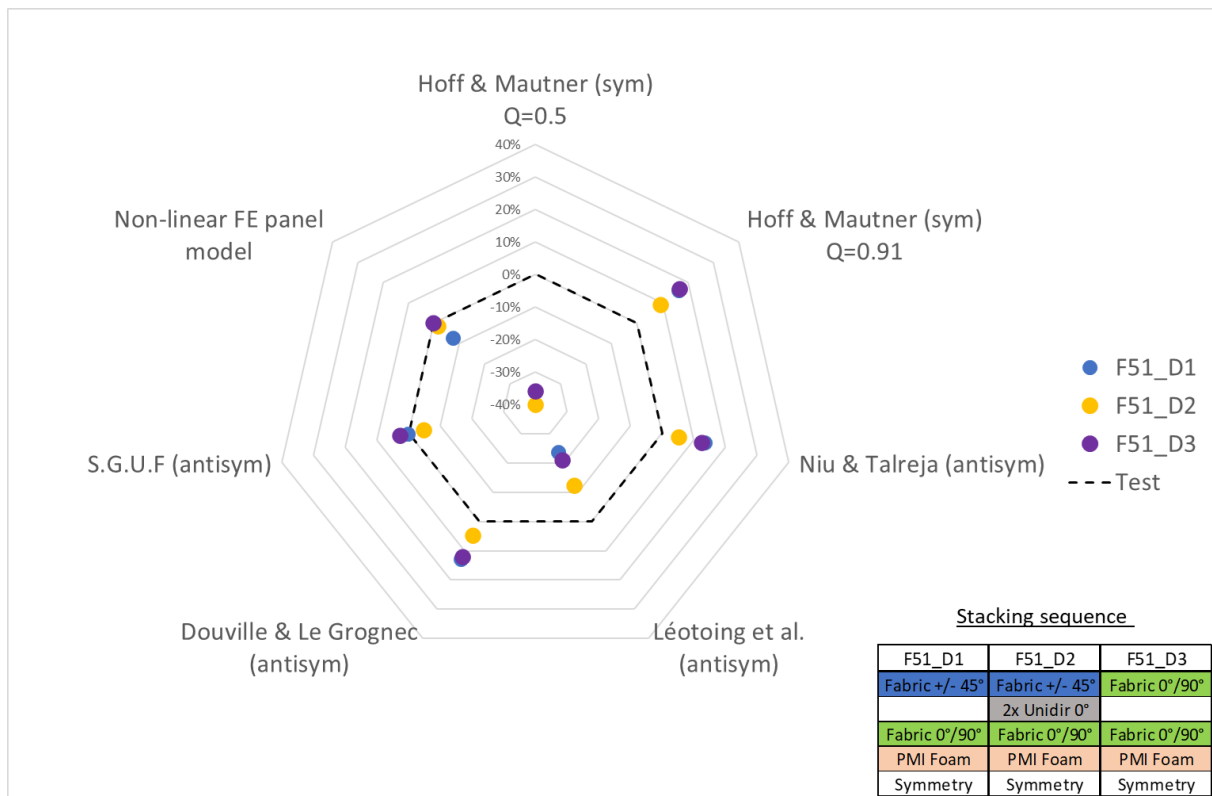


Figure 26: Radar comparison graph between models and test results.

639
640
641
642
643
644
645
646
647
648
649
650

The advanced nonlinear FE panel model provides an improved and conservative prediction of wrinkling loads over the linear models. The integration of initial imperfections in the mesh and a constitutive law for the core is effective to obtain correlation with the experimental results. Nevertheless, the failure load computed by the non-linear FE panel model is quite similar to the critical load computed by the linear S.G.U.F model. In this study, the strength issue and the stability problem are not so different. But a particular effort has been made on the quality of the specimens, where the maximum amplitude of the initial imperfections has been measured at about 10% of the thickness of the sandwiched panel (Ginot et al., 2023). In an industrial application, the imperfections may be greater and the difference between the two approaches may be significant.

651 6 Conclusions

652 An exhaustive experimental and computation dialogue on local buckling, named “wrinkling”,
653 in sandwich panels has been performed in this paper. The test results of three sandwich panels
654 bolted on four sides and tested in compression and shear using the VERTEX test bench have
655 been compared to models. Stacking sequences and material properties (orthotropic
656 asymmetric carbon skins and foam core) are in accordance with an industrial application in
657 light aviation.

658 Firstly, linear 2D plane strain models are challenged with test results. Analytical formulas show
659 optimistic correlations with test results. Beyond a framework (3D stress state; skin orthotropy;
660 bi-modulus behaviour in the core) far from the assumptions on which they were based, these
661 models do not take the initial imperfections into account, which can seriously lower failure
662 loads according to the literature. For specimen F51_D3 tested in shear, the correlation is of
663 the same order as for the specimens tested in compression. This demonstrates that models
664 based on uniaxial loading can be used in shear.

665 Then an advanced non-linear Finite Elements Model of the sandwich panels has been
666 developed. The SDIC measurement data allows the initial shape of the upper face of the
667 sandwich panel to be directly integrated into the FE mesh. Little ripples, considered as
668 imperfections, induce a non-linear local response generating out-of-plane displacements that
669 affect local in-plane and out-of-plane strains. This triggers the failure of the core material. This
670 observation leads to a refinement of the core behaviour. A constitutive law for the core is
671 implemented in the principal directions. The law is isotropic with bi-modulus behaviour. A
672 perfect elastoplasticity model is used for compression and an elastic response with damage

673 modelled by element deletion is used for tension. Due to convergence issues, the choice of
674 the dynamic explicit computation is made and run using the explicit solver ABAQUS. The
675 integration of initial imperfections in the mesh allows the buckling in the sandwich panel to
676 be localised. This is observed in tests. Moreover, the constitutive law for the core with failure
677 prediction (crushing and tensile failure) allows the strength approach whereas a linear
678 analytical stability approach is too optimistic (10% on average). The evolution of in-plane
679 strains in the wrinkling area with the local buckling onset is well represented in the
680 simulations.

681 The advanced non-linear FEM of the sandwich panels provides a remarkable prediction of
682 wrinkling compared to the experiment results. However, the model is the result of extensive
683 work on mesh construction, loading condition, and nonlinear material modelling with the use
684 of a dynamic explicit solver. This would not be possible without extensive instrumentation of
685 the tests and the measurement fields offered by the SDIC. In this sense, we have moved away
686 from the means and time available to the engineer for his design. Such a model would be
687 difficult to implement in an industrial context. The linear S.G.U.F model (D'Ottavio and Polit,
688 2015), which is much simpler and applicable to industrial design, also correlates well with the
689 test results. A safety approach could be used with knock down factors in the mechanical
690 characteristics of the core and/or the thickness of the skins. Both are preponderant in the
691 occurrence of wrinkling. This approach, in particular on the thickness, is widely used by the
692 industry for the calculation of buckling of shell structures by global finite element models
693 (GFEM). Similarly, Niu and Talreja, (1999) and Douville and Le Grogneq, (2013) analytical
694 models can be used with a knock down factor. In general, for analytical models, the

695 assumptions used should be carefully checked so that the theoretical framework does not
696 deviate too much from the real one.

697 **Declaration of Competing Interest**

698 The authors declare that they have no known competing financial interests or personal
699 relationships that could have appeared to influence the work reported in this paper.

700 **Acknowledgements**

701 This research is part of a CIFRE PhD thesis in collaboration with the aircraft manufacturer Elixir
702 Aircraft (<https://elixir-aircraft.com>). This work was partially funded by the “Fondation Jean-
703 Jacques et Felicia Lopez-Loreta pour l’Excellence Académique” as part of the VIRTUOSE
704 (VIRTual testing of aerOnautical StructurEs) project ([https://websites.isae-
705 supaero.fr/virtuose/](https://websites.isae-supaero.fr/virtuose/)). The authors gratefully acknowledge CALMIP (CALcul en MidiPyrénées,
706 <https://calmip.univ-toulouse.fr>) for access to the HPC resources and the fast and effective
707 computations it allows. The authors would also like to thank C3Technologies
708 (<http://www.c3technologies.fr>) for the quality of the sandwich specimens they manufactured.

709 **References**

- 710 Abaqus Analysis user’s manual, Dassault Systemes Simulia, V6.12. chap 11.6.1 Mass scaling.
711 [http://193.136.142.5/v6.12/books/usb/default.htm?startat=pt04ch11s06aus74.html#u
712 sb-anl-amassscaling](http://193.136.142.5/v6.12/books/usb/default.htm?startat=pt04ch11s06aus74.html#usb-anl-amassscaling)
- 713 Abrate, S., 2008. Criteria for yielding or failure of cellular materials. *J. Sandw. Struct. Mater.*
714 10, 5–51. <https://doi.org/10.1177/1099636207070997>
- 715 Allen, H.G., 1969. Wrinkling and other forms of local instability, in: Neal, B.. (Ed.), *Analysis*
716 *and Design of Structural Sandwich Panels*. [https://doi.org/10.1016/b978-0-08-012870-
717 2.50012-2](https://doi.org/10.1016/b978-0-08-012870-2.50012-2)
- 718 Arbocz, J., 1982. Imperfection Data Bank, a Mean To Obtain Realistic Buckling Loads., in:
719 Ramm, E. (Ed.), *Buckling of Shells*. pp. 535–567. <https://doi.org/10.1007/978-3-642->

720 49334-8_19

721 ASTM C297, 2004. Standard Test Method for Flexural Properties of Sandwich Constructions.

722 ASTM C365, 2011. Standard Test Method for Flatwise Compressive Properties of Sandwich
723 Cores.

724 Benson, A.S., Mayers, J., 1967. General Instability and Face Wrinkling of Sandwich Plates
725 Unified Theory and Applications. *AIAA J.* 5(4), 729-739. <https://doi.org/10.2514/3.4054>

726 Birman, V., Bert, C.W., 2004. Wrinkling of composite-facing sandwich panels under biaxial
727 loading. *J. Sandw. Struct. Mater.* 6, 217–237.
728 <https://doi.org/10.1177/1099636204033643>

729 Bisagni, C., 2000. Numerical analysis and experimental correlation of composite shell
730 buckling and post-buckling. *Compos. Part B Eng.* 31, 655–667.
731 [https://doi.org/10.1016/S1359-8368\(00\)00031-7](https://doi.org/10.1016/S1359-8368(00)00031-7)

732 Castanié, B., Barrau, J.J., Jaouen, J.P., 2002. Theoretical and experimental analysis of
733 asymmetric sandwich structures. *Compos. Struct.* 55, 295–306.
734 [https://doi.org/10.1016/S0263-8223\(01\)00156-8](https://doi.org/10.1016/S0263-8223(01)00156-8)

735 Castanié, B., Bouvet, C., Ginot, M., 2020. Review of composite sandwich structure in
736 aeronautic applications. *Compos. Part C Open Access* 1, 100004.
737 <https://doi.org/10.1016/j.jcomc.2020.100004>

738 D’Ottavio, M., 2016. A Sublaminar Generalized Unified Formulation for the analysis of
739 composite structures. *Compos. Struct.* 142, 187–199.
740 <https://doi.org/10.1016/j.compstruct.2016.01.087>

741 D’Ottavio, M., Polit, O., 2015. Linearized global and local buckling analysis of sandwich struts
742 with a refined quasi-3D model. *Acta Mech.* 226, 81–101.
743 <https://doi.org/10.1007/s00707-014-1169-2>

744 D’Ottavio, M., Polit, O., Ji, W., Waas, A.M., 2016. Benchmark solutions and assessment of
745 variable kinematics models for global and local buckling of sandwich struts. *Compos.*
746 *Struct.* <https://doi.org/10.1016/j.compstruct.2016.01.019>

747 Deshpande, V.S., Fleck, N.A., 2000. Isotropic constitutive models for metallic foams. *J. Mech.*
748 *Phys. Solids* 48, 1253–1283. [https://doi.org/10.1016/S0022-5096\(99\)00082-4](https://doi.org/10.1016/S0022-5096(99)00082-4)

749 Douville, M.A., Le Grogneq, P., 2013. Exact analytical solutions for the local and global
750 buckling of sandwich beam-columns under various loadings. *Int. J. Solids Struct.* 50,
751 2597–2609. <https://doi.org/10.1016/j.ijsolstr.2013.04.013>

752 Elixir Aircraft. <https://elixir-aircraft.com>

753 Fagerberg, L., 2004. Wrinkling and compression failure transition in sandwich panels. *J.*
754 *Sandw. Struct. Mater.* 6, 129–144. <https://doi.org/10.1177/1099636204030475>

755 Fagerberg, L., Zenkert, D., 2005a. Effects of anisotropy and multiaxial loading on the
756 wrinkling of sandwich panels. *J. Sandw. Struct. Mater.* 7, 177–194.
757 <https://doi.org/10.1177/109963205048525>

758 Fagerberg, L., Zenkert, D., 2005b. Imperfection-induced wrinkling material failure in
759 sandwich panels. *J. Sandw. Struct. Mater.* 7, 195–219.
760 <https://doi.org/10.1177/1099636205048526>

761 Featherston, C.A., Eaton, M.J., Holford, K.M., 2012. Modelling the effects of geometric
762 imperfections on the buckling and initial post-buckling behaviour of flat plates under
763 compression using measured data. *Strain* 48, 208–215. [https://doi.org/10.1111/j.1475-](https://doi.org/10.1111/j.1475-1305.2011.00813.x)
764 [1305.2011.00813.x](https://doi.org/10.1111/j.1475-1305.2011.00813.x)

765 Gibson, L.J., Ashby, M.F., 1997. *Cellular solids*. Cambridge University Press.
766 [https://doi.org/10.1016/0021-9290\(89\)90056-0](https://doi.org/10.1016/0021-9290(89)90056-0)

767 Ginot, M., Bouvet, C., Castanié, B., Serra, J., Mahuet, N., 2023. Local buckling on large
768 sandwich panels applied to light aviation: Experimental setup and failure scenarios.
769 *Compos. Struct.* 304. <https://doi.org/10.1016/j.compstruct.2022.116439>

770 Ginot, M., D’Ottavio, M., Polit, O., Bouvet, C., Castanié, B., 2021. Benchmark of wrinkling
771 formulae and methods for pre-sizing of aircraft lightweight sandwich structures.
772 *Compos. Struct.* 273, 114387. <https://doi.org/10.1016/j.compstruct.2021.114387>

773 Hoff, N.J., Mautner, S.E., 1945. The Buckling of Sandwich-Type Panels. *J. Aeronaut. Sci.* 12,
774 285–297. <https://doi.org/10.2514/8.11246>

775 Huo, X., Jiang, Z., Luo, Q., Li, Q., Sun, G., 2022. Mechanical characterization and numerical
776 modeling on the yield and fracture behaviors of polymethacrylimide (PMI) foam
777 materials. *Int. J. Mech. Sci.* 218. <https://doi.org/10.1016/j.ijmecsci.2021.107033>

778 Kassapoglou, C., 2010. *Design and Analysis of Composites Structures*. Wiley.

779 Kassapoglou, C., Fantle, S.C., Chou, J.C., 1995. Wrinkling of composite sandwich structures
780 under compression. *J. Compos. Technol. Res.* 17, 308–316.
781 <https://doi.org/10.1520/ctr10451j>

782 Leotoing, L., 2001. *Modélisation Du Flambage Global, Local et Interactif Dans Les Structures*
783 *Sandwich En Compression*. PhD Mines de Saint-Etienne, France.
784 <https://www.theses.fr/2001EMSE0020>

785 Léotoing, L., Drapier, S., Vautrin, A., 2002. Nonlinear interaction of geometrical and material
786 properties in sandwich beam instabilities. *Int. J. Solids Struct.* 39, 3717–3739.
787 [https://doi.org/10.1016/S0020-7683\(02\)00181-6](https://doi.org/10.1016/S0020-7683(02)00181-6)

788 Ley, R.P., Lin, W., Mbanefo, U., 1999. Facesheet wrinkling in sandwich structures, NASA/CR-
789 1999-208994.
790 <https://ntrs.nasa.gov/api/citations/19990017863/downloads/19990017863.pdf>

791 Niu, K., Talreja, R., 1999. Modeling of wrinkling in sandwich panels under compression. *J.*
792 *Eng. Mech.* 125, 875–883. [https://doi.org/10.1061/\(ASCE\)0733-9399\(1999\)125:8\(875\)](https://doi.org/10.1061/(ASCE)0733-9399(1999)125:8(875))

793 Norris, C.B., 1964. Short-column compressive cf strength of sandwich constructions as
794 affected by size of cells of honeycomb core materials. *For. Prod. Lab. For. Serv. U.S.*
795 *Dep. Agric.* <https://doi.org/10.1007/BF00731082>

- 796 Pinho, S., 2005. Modelling composites failure laminated of using physically-based failure
797 models. PhD Imperial College London, UK.
798 <https://paginas.fe.up.pt/~stpinho/research/past/phd/>
- 799 Plantema, F. J., 1966. Sandwich Construction: The Bending and Buckling of Sandwich Beams,
800 Plates and Shells, John Wiley and Sons.
- 801 Serra, J., Bouvet, C., Castanié, B., Petiot, C., 2016. Scaling effect in notched composites: The
802 Discrete Ply Model approach. *Compos. Struct.* 148, 127–143.
803 <https://doi.org/10.1016/j.compstruct.2016.03.062>
- 804 Serra, J., Pierré, J.E., Passieux, J.C., Périé, J.N., Bouvet, C., Castanié, B., 2017a. Validation and
805 modeling of aeronautical composite structures subjected to combined loadings: The
806 VERTEX project. Part 1: Experimental setup, FE-DIC instrumentation and procedures.
807 *Compos. Struct.* 179, 224–244. <https://doi.org/10.1016/j.compstruct.2017.07.080>
- 808 Serra, J., Pierré, J.E., Passieux, J.C., Périé, J.N., Bouvet, C., Castanié, B., Petiot, C., 2017b.
809 Validation and modeling of aeronautical composite structures subjected to combined
810 loadings: The VERTEX project. Part 2: Load envelopes for the assessment of panels with
811 large notches. *Compos. Struct.* 180, 550–567.
812 <https://doi.org/10.1016/j.compstruct.2017.08.055>
- 813 Serra, J., Trellu, A., Bouvet, C., Rivallant, S., Castanié, B., Ratsifandrihana, L., 2021. Combined
814 loadings after medium velocity impact on large CFRP laminated plates: Discrete ply
815 model simulations. *Compos. Part C Open Access* 6.
816 <https://doi.org/10.1016/j.jcomc.2021.100203>
- 817 Stiftinger, M.A., Rammerstorfer, F.G., 1997. Face layer Wrinkling in sandwich shells -
818 Theoretical and experimental investigations. *Thin-Walled Struct.* 29, 113–127.
- 819 Sullins, R.T., Smith, G.W., Spier, E.E., 1969. Manual for structural stability analysis of
820 sandwich plates and shells. NASA Contract. Reports CR-1457.
821 <https://ntrs.nasa.gov/citations/19700004831>.
- 822 Sztefek, P., Olsson, R., 2008. Tensile stiffness distribution in impacted composite laminates
823 determined by an inverse method. *Compos. Part A Appl. Sci. Manuf.* 39, 1282–1293.
824 <https://doi.org/10.1016/j.compositesa.2007.10.005>
- 825 Thomsen, O.T., Rits, W., Eaton, D.C.G., Brown, S., 1996a. Ply drop-off effects in
826 CFRP/honeycomb sandwich panels - Theory. *Compos. Sci. Technol.* 56, 407–422.
827 [https://doi.org/10.1016/0266-3538\(95\)00145-X](https://doi.org/10.1016/0266-3538(95)00145-X)
- 828 Thomsen, O.T., Rits, W., Eaton, D.C.G., Dupont, O., Queekers, P., 1996b. Ply drop-off effects
829 in CFRP/honeycomb sandwich panels - Experimental results. *Compos. Sci. Technol.* 56
830 56, 423–437. [https://doi.org/https://doi.org/10.1016/0266-3538\(96\)00007-3](https://doi.org/https://doi.org/10.1016/0266-3538(96)00007-3)
- 831 Trellu, A., Pichon, G., Bouvet, C., Rivallant, S., Castanié, B., Serra, J., Ratsifandrihana, L., 2020.
832 Combined loadings after medium velocity impact on large CFRP laminate plates: Tests
833 and enhanced computation/testing dialogue. *Compos. Sci. Technol.* 196, 23.
834 <https://doi.org/10.1016/j.compscitech.2020.108194>

- 835 Tuwair, H., Volz, J., ElGawady, M.A., Chandrashekhara, K., Birman, V., 2016. Modeling and
836 Analysis of GFRP Bridge Deck Panels Filled with Polyurethane Foam. *J. Bridg. Eng.* 21,
837 04016012. [https://doi.org/10.1061/\(asce\)be.1943-5592.0000849](https://doi.org/10.1061/(asce)be.1943-5592.0000849)
- 838 Vescovini, R., D'Ottavio, M., Dozio, L., Polit, O., 2018. Buckling and wrinkling of anisotropic
839 sandwich plates. *Int. J. Eng. Sci.* 130, 136–156.
840 <https://doi.org/10.1016/j.ijengsci.2018.05.010>
- 841 Vonach, W.K., Rammerstorfer, F.G., 2000. Wrinkling of thick orthotropic sandwich plates
842 under general loading conditions. *Arch. Appl. Mech.* 70, 338–348.
843 <https://doi.org/10.1007/s004199900065>
- 844 Wagner, H.N.R., Hühne, C., Elishakoff, I., 2020. Probabilistic and deterministic lower-bound
845 design benchmarks for cylindrical shells under axial compression. *Thin-Walled Struct.*
846 146, 106451. <https://doi.org/10.1016/j.tws.2019.106451>
- 847 Wang, J., Wang, H., Chen, X., Yu, Y., 2010. Experimental and numerical study of the elastic
848 properties of PMI foams. *J. Mater. Sci.* 45, 2688–2695. [https://doi.org/10.1007/s10853-](https://doi.org/10.1007/s10853-010-4250-9)
849 [010-4250-9](https://doi.org/10.1007/s10853-010-4250-9)
- 850 Xin, R., Le, V.T., Goo, N.S., 2022. Buckling identification in composite cylindrical shells with
851 measured imperfections using a Multi-DIC method and finite element analysis. *Thin-*
852 *Walled Struct.* 177, 109436. <https://doi.org/10.1016/j.tws.2022.109436>
- 853 Zenkert, D., 1997. *The handbook of the sandwich construction.* Engineering Materials
854 Advisory Services.
- 855